CHARACTERIZATION OF HIGH EFFICIENCY PSEUDO BILAYER ORGANIC SOLAR CELLS AND IDENTIFICATION OF TRAP-STATES WITH A MODIFIED CELIV TECHNIQUE

LAXMI NARASIMHA SAI ABHINAND THUMMALAKUNTA

(*B.ENG, NUS*)

A THESIS SUBMITED FOR THE DEGREE OF MASTERS OF ENGINEERING FROM THE DEPARTMENT OF CHEMICAL AND BIOMOLECULAR ENGINEERING

NATIONAL UNIVERSITY OF SINGAPORE

2014

Declaration

I hereby declare that this thesis is my original work and it has been written by me in its entirety. I have duly acknowledged all the sources of information which have been used in the thesis.

This thesis has also not been submitted for any degree in any university previously.

Laxmi Narasimha Sai Abhinand Thummalakunta

14th August 2014

Acknowledgments

The work presented in this dissertation is based on my research experience in the National University of Singapore. This experience was very enriching and memorable and I would like to express my deepest gratitude to a few individuals who made this experience possible. I would like to thank my supervisor, Dr. Karl Erik Birgersson, allowing me to independently pursuing my passions, and giving me timely guidance. I am also grateful to Associate Professor Peter Ho for extending support to our group during an unfortunate circumstance that SERIS was put under. I am also very thankful to Professor Jochim Luther for his invaluable belief in my scientific capabilities and also for his regular scientific inputs in my research work.

Apart from that, I am very grateful to all the scientific facilities and man power provided by SERIS. Financial support in the form of research assistant's job provided by SERIS to me had been invaluable and is much appreciated.

My special thanks to the staff, colleagues and friends at SERIS and Chemical and Biomolecular Engineering Department with whom I have had the privilege to read and work with. Some of the people that require a special mention are: Dr. K. Ananthanarayanan, Ying Ting Set, Lim Fang Jeng, Yong Chian Haw, Dr. Wong Kim Hai, Thomas Gascou and Marc Daniel Heinemann. Their help has been invaluable in completing my experiments and having inspiring scientific discussions.

Finally, I would like to express my deepest thanks to my parents, brother and friends for their unconditional love and support through my rough patches

TABLE OF CONTENTS

Summary

Firstly, this thesis investigates a novel Organic Solar Cell (OSC) fabrication technique with the use of a new acceptor material, indene-C60 bisadduct (ICBA). Once the solar cell was fabricated, an investigation was made to find out the reason behind an increased device performance due to annealing. The investigation revealed that the improved performance was due to the heat energy being used up in crystallizing the acceptor material (ICBA) thereby improving the charge transport properties of electrons in the solar cell.

Secondly, the thesis also investigates the degradation of polymer OSCs made from poly (3-hexylthiophene) (P3HT) and phenyl-C61-butyric acid methyl ester (PCBM). It introduces a new transient technique, called the LB-CELIV that can quickly identify trap-states in an OSC. This technique if implemented can act as an efficient prognostic tool that can be industrially used to weed out underperforming solar cells for an inline manufacturing setup.

Apart from that, a steady state numerical model was developed to explain J-V characteristics of OSCs. A general transient model was later developed that can simulate various transient experiments (such as transient photocurrent, transient photovoltage etc.). This model was then used to simulate LB-CELIV and then validate various experimental findings. The model was also used to fit some experimental data and evaluate various important device parameters such as electron or hole mobilities, trap-state concentration, etc.

Nomenclature

OSC	Organic solar cell

CELIV	Charge extraction by a linearly increasing voltage pulse
P3HT	poly (3-hexylthiophene)
PCBM	phenyl-C61-butyric acid methyl ester
ICBA	Indene-C60 bisadduct
J-V	Current density and voltage measurements
PL	Photoluminescence
EQE	External Quantum Efficiency
PET	Polyethylene terephthalate
PV	Photovoltaic
PCE	Power conversion efficiency
TCO	Transparent conducting oxide
ITO	Tin doped indium oxide
PEDOT:PSS	Poly(3,4-ethylenedioxythiophene) Polystyrene sulfonate

List of Publications

- "P3HT based solution-processed pseudo bi-layer organic solar cell with enhanced performance", L.N.S.A. Thummalakunta, C. H. Yong, K. Ananthanarayanan, J. Luther, Organic Electronics, 13 (2012) 2008–2016.
- "Identification of trap-states in organic solar cells by means of a modified Photo-CELIV technique ", L.N.S.A. Thummalakunta, J. Luther and E. Birgersson (Manuscript in preparation)

List of Figures

List of Tables

Chapter 1

Introduction

After accounting for the sunlight scattered and obsorbed by the earth's atmosphere, it has been calculated that a total of about 175 W/m^2 [1] is received by the earth every day. It can from here be calculated that the energy received by the earth in 1.5 hrs is more than the total consumption of the world in the year 2001. This comparison gives you an idea of the enormity of the energy that the earth receives from the sun. This is the reason why solar energy has recently received so much of attention. Among all the other natural sources (alternative sources) of energy, solar energy has, by far, highest potential of sustaining the growing energy need of our world.

Among other forms of energy, electricity forms the crux of the energy crisis in the world today and solar cells help solve this problem by converting the sunlight into electricity. These modern silicon based solar cells were first made during the 1950s in Bell labs [2]. They however since then have generally suffered from high cost. For example, the cost of high power band solar modules (a collection of a few solar cells) was about USD$ 27,000/kW in 1982 and the cost of installing a photovoltaic (PV) system in 1992 was around USD$ 16,000 [3]. This relatively high cost of manufacturing and installing solar cells had initially restricted the use of solar cells only for high cost projects such as powering a satellite in outer space. However, as time progressed, the prices of module production had come down to USD $ 4,000/kW (2006), installing came down to USD $ 6,000 (2008) and in 2014, cell cost had come down to as low as USD $350/kW. This sudden decrease has fuelled the growth of the solar industries as can be seen from increased government investing, introduction of newer subsidies and higher research and development (R&D) budgets for solar energy. Reports have shown that global PV installations increased from 1.4 GW in 2000 to 40 GW in 2010 [3] and installed capacity only seems to keep increasing as the $/W ration keeps decreasing. In India alone, at the end of 2013, a total of 2018 GW worth of PV installations were made.

This is almost a 100% increment from its values at the end of 2012 [4]. Singapore on the other hand, with a high solar irradiation (amount of solar energy received by earth) of 1,150 kWh/kW_p/year that is 50% more than what its temperate counter parts receive [5] has an installed total capacity of 14.7461 MW_p as of 2014. This is a phenomenal increment compared to its installed capacity of 0.3619 MW_p in 2009 [6].

It is evident that solar energy is a clean source of energy but to make it more desirable for the end users, it is needs to be more economical. This means that the cost of producing energy from solar energy is lesser than or equal to the price of purchasing power from the electricity grid. If this condition is met, then, it is said that grid parity is attained and that this alternative source of energy is now a contender for widespread use without and subsidies or governmental support. It was attained in Australia in 2011 [7] and is increasingly being attained at other parts of the world too.

The above stated reasons are why it is very important to do more research in the field of solar energy as even a small improvement in the power conversion efficiency (PCE – amount of solar energy converted to electrical power by a solar cell) of the solar cells could mean a vast amount of energy produced which in turn would save a vast amount of fossil fuels that would have otherwise been used up in producing that energy.

Types of Solar Cells

Let us now discuss about the most important types of solar cells that exist in the current market. As can be seen in Figure 1, the highest power conversion efficiency attained by a solar cell is 44.4% and this is attained by a three-junction solar cell. However, multi-crystalline silicon solar modules account for 62% of all modules produced in the current market. Next major share is taken by thin film technology (such as amorphous silicon, CIGS, etc.) which stands at 8.9% this year [8,9].

The above described technologies are relatively old and have been researched upon for a long time. There have been, however, more recent technologies that have shown a lot of potential such as dye sensitized solar cells, perovskite solar cells and organic solar cells. There is a lot of research that is being carried out on them to increase their device efficiencies and life times.

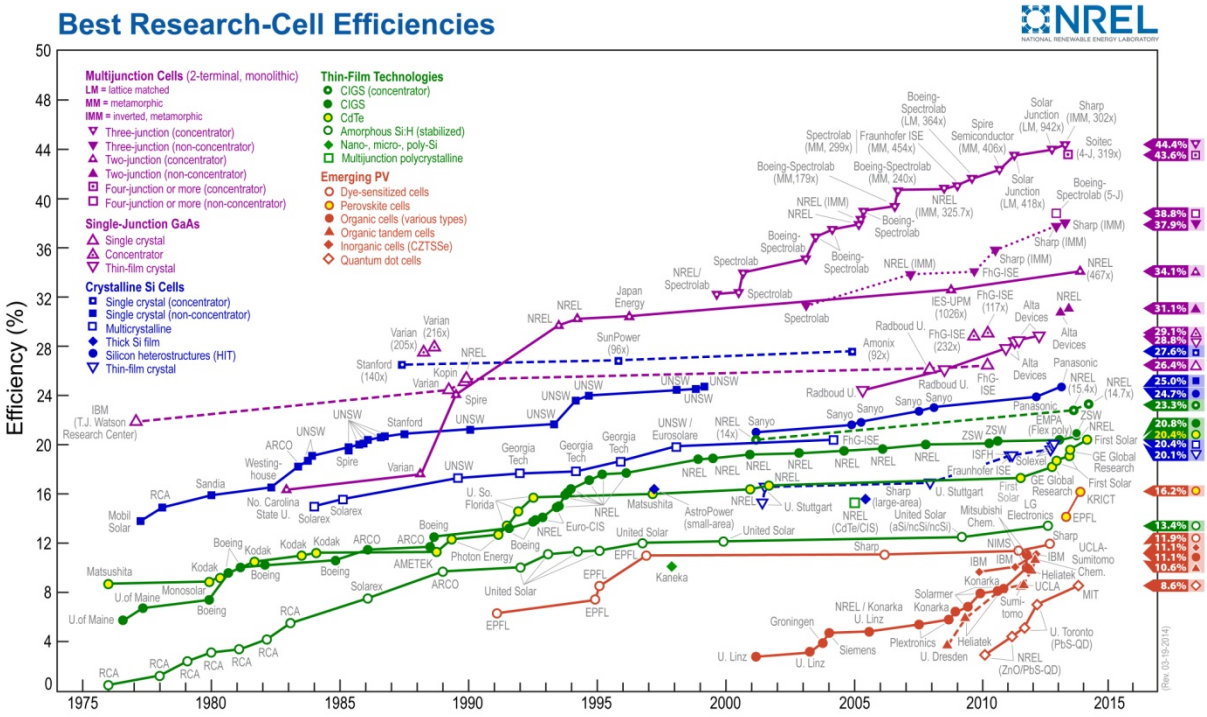

Figure 1 A collection of record certified PV efficiencies of various PV technologies vs the year of their certification.

Crystalline silicon solar cells

In 2008, the world annual PV power production had reached beyond 7.9 GW_p (W_p, peak power under standard test conditions) [32], and the average annual growth rate of PV cell production over the last decade has been more than 40%. Yet electrical power generated by all PV systems around the world has been estimated to be less than 0.1% of the total world electricity generation [32]. Still, the strong growth in PV cell production is expected to continue for many years due to the sheer increase in PV module installations. Crystalline silicon PV cells, with over 60 years of research, have the longest production history and now

account up to 90% of all solar cells produced in 2008 [32]. Some of the reasons why silicon is used widely for solar applications are because it is safe for the environment and one of the most abundant resources on Earth, representing 26% of the crustal material. World annual PV cell production of 100 GW_p is expected to be achieved by around 2020, and at the moment, the silicon PV cell seems to be the most viable candidate to meet this demand from the point of view of large-volume production.

Before looking into the working of a crystalline solar cell, let us look at how these crystalline silicon wafers are fabricated. Most silicon cells are fabricated from thin silicon wafers that are cut from large cylindrical mono-crystalline silicon ingots that are prepared from the Czochralski (CZ) crystal growth process that is doped with boron (1 part per billion) during its ingot growth. Next, to produce a working solar cell, these boron doped (*p*-type) wafers are then exposed to phosphorus (*n*-type) that is diffused into the wafer at high temperatures. Hence, at this point, these wafers have highly phosphorous-doped n_+ (electron-producing) regions on the front surface of boron-doped *p*-type (electron-accepting) substrates to form a *p–n* junction. Back-surface p_+ field (BSF) regions of the wafer are formed to suppress recombination of minority carriers (photo-generated electrons). These regions are usually formed by firing screen-printed aluminium paste in a belt furnace. The carriers (electrons) generated in the silicon bulk and diffusion layers are, however, collected by silver contacts formed on the front and back silicon surfaces. The front contact consists of gridlines connected by a bus-bar to form a comb-shaped structure. The back contact is usually a series of silver stripes connected to the front bus-bar of the adjacent cell via soldered copper interconnects. This, in brief, is how a crystalline solar cell is fabricated.

The main advantages that these solar cells posses, as discussed before, are that they are environmentally friendly and that the raw materials required are very abundant. The other advantages with this technology are that they possess high, industrially relevant, power

conversion efficiency [34] and that they have a lot of research history [33]. At the same time, the disadvantages that plague the technology are that the modules are very heavy [35] and is hence tough to transport and that the solar cell fabrication techniques requires the use of high vacuum systems, high temperature fabrication procedures [36] and a lot of expensive materials such as silver (for electrode contacts) which invariably increases the process time and cost.

Amorphous silicon solar cells

Bonding of atoms in non-crystalline (amorphous) silicon is nearly unchanged from that of its crystalline counter parts. Nonetheless, a fairly small, disorderly variation in the angles between bonds eliminates the regularity in the lattice structure. Though they posses such non regularities, they still have fairly good electronic properties sufficient for many applications. One of the applications is to make solar cells of the amorphous kind. In 1973, Walter Spear and Peter LeComber discovered that amorphous silicon prepared using a "glow discharge" in silane (SiH_4) gas unusually had good electronic properties. This work was built on earlier work done by Chittick, Sterling, and Alexander [10]. An electric voltage is applied across a gas can to induce a significant electrical current through the gas, and the molecules of the gas often emit light when excited by the current forming the "glow discharge". Amorphous silicon was deposited as a thin film by this technique with silane gas. Later in 1975, Spear and LeComber reported an enormous increment in conductivity [11] when the silane gas is mixed with phosphine (PH_3) gas or some diborane (B_2H_6) gas. It was found out that the increased conductivity is associated with p-doping (by B_2H_6) and n-doping (by PH_3) of amorphous silicon. In 1976, the first amorphous silicon solar cell was made by David Carlson and Christopher Wronski and its efficiency was 2.4% [12]. When amorphous silicon solar cells were made by, for example, evaporation of silicon, the device efficiencies were not as good as they can get by doing plasma coating or "glow discharge" coating. It was later found

out that the improved efficiency was mainly attributed to the hydrogen that got bounded to the pre-existing silicon and this was why the device performance significantly increased and so since then, hydrogenated amorphous silicon solar cells came to be known as amorphous silicon solar cells (a-Si-H).

The advantages with a-Si-H solar cells are that fabrication procedure is much simpler and cheaper when compared to crystalline silicon solar cells. Apart from that, a-Si-H solar cells can absorb more light for the same layer thickness than a crystalline silicon solar cell which means that much lesser material is used in making an efficient solar cell.

Now let us understand how a simple a-Si-H solar cell works. It is generally made in a *p*-*i*-*n* (*p*-doped material – intrinsic material – *n*-doped material) fashion where a transparent conducting oxide (TCO) layer has a thin *p*-doped deposited underneath a thick intrinsic (*i*) layer finally capped off by a thin *n*-doped layer and the back reflector. As illustrated in Figure 2, *p*-doped layer gives up holes and *n*-doped layer gives up electrons. These excess free charges now reside in the *n*-doped and *p*-doped layers causing an inherent charge build-up to occur in the device. As a result, a huge electric field is built inside the device. So when the sunlight enters the photodiode (TCO) as a stream of photons, they pass through the *p*-doped layer, which is a nearly transparent. The solar photons are then mostly absorbed by the much thicker intrinsic layer. Each absorbed photon will generate an electron and a hole [14]. The photo-generated charge carriers are then swept away by the built-in electric field to the *n*-doped and *p*-doped layers thus generating current. This is briefly how a-Si-H solar cells function.

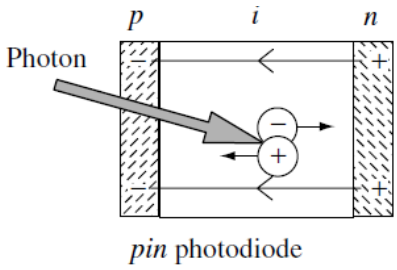

Figure 2 A correctional view of an a-Si-H solar cell

The main disadvantage of this technology is that their current single junction device efficiency is reaching just beyond 10% and a theoretical limit of between 15%-22% [15] is expected for these devices. This is less than its crystalline silicon counter parts. Other than that, another major drawback with this technology is that the devices are not very stable and they degrade over time [16].

Dye sensitized solar cells

Dye sensitized solar cells (DSSCs) are one of the new breed of solar cells that are currently been researched about. At the heart of a DSSC is a mesoporous oxide layer composed of nanometer-sized particles that have been sintered together to allow for electronic conduction to take place. The material of choice has usually been TiO_2 (anatase) although alternative wide band gap oxides such as ZnO [17] and Nb_2O_5 [18] have also been previously used in making devices. Attached to the surface of the nanocrystalline film is a monolayer of photoexcitable dye. Photo excitation of this dye results in the injection of an electron into the conduction band of the metal oxide. The original state of the dye is then restored by electron donation from the electrolyte, usually an organic solvent such as acetonitrile containing a redox system, such as the iodide/triiodide couple. The regeneration of the sensitizer by iodide prevents the recapture of the conduction band electron by the oxidized dye. The iodide used up at the dye is regenerated in turn by the reduction of the triiodide species at the counter electrode where the electron that migrates through the external load is used up when it

reaches the counter electrode. Overall the device generates electric power from light without suffering any permanent chemical transformation.

DSSCs have been in the research community since before 1991 but it was in this year that Prof. Gratzel had first fabricated an extremely efficient DSSC (7.1%). Since then, the PCEs of these devices had gradually increased. In 2010, liquid electrolyte based DSSCs had reached PCEs of around 11.8%. However, DSSCs were still having problems with their stability due to liquid electrolytes being used as a hole transport medium. In order to overcome this, research on solid state DSSCs was started since 1998. The major contender for this breed of DSSCs were the once made from the solid hole transport material (HTM (electrolyte)), spiro-MeOTAD. These DSSCs reached an efficiency of around 6% and in order to further increase this number, a dopant was added into the spiro-MeOTAD to make it more conducting (almost one order of magnitude increase in conductivity was observed) there by increasing the device efficiency to 7.2% [19]. This value was further increased by the use of perovskite sensitizers (as a replacement to the commonly used Ruthenium dyes).

The main disadvantage of this technology is that it is quite expensive owing to the two TCOs it takes to fabricate this solar cell. Upon doing a cost analysis on a DSSC, it has been found out that 67% [20] of the production cost comes from the TCO and hence using two such TCOs has made the production cost very high. The other disadvantage is that a DSSC uses liquid electrolytes to obtain the best ion/charge mobility. At high temperatures, liquid electrolyte expands making it hard to seal the sample and at lower temperatures, the electrolyte freezes, ending power production and potentially leading to physical damage. This puts the cell into temperature instability. Apart from that, liquid electrolyte is found to be very corrosive in nature, photo-reactive and is also found to react with the metal electrode material and the sealant [22]. Sold state electrolytes were supposed to overcome at least some of these disadvantages and they do a good job of it but due to poor interface contact and

lower conductivity for solid state electrolytes, a lower PCE is observed for DSSCs [21]. Another major drawback is that the electrolyte solution contains volatile organic compounds (or VOC's), solvents which must be carefully sealed as they are hazardous to human health and the environment [23]. These are some of the challenges that this technology is facing.

Perovskite Solar Cells

In 2012, organometal halide, $CH_3NH_3PbI_3$ having the perovskite structure was adsorbed onto a sub-micrometer thick mesoporous TiO_2 film and a solar cell made out of this had exhibited a PCE of 9.7% under 1 sun illumination [24]. The device is very similar to a conventional DSSC but instead of a dye sensitizer, perovskite sensitizers are used instead. The device was later stored for 500 hours in air at room temperature without encapsulation and it still retained its full photovoltaic performance. Next, high-efficiency solid-state solar cell was also developed almost at the same time using a $CH_3NH_3PbI_2Cl$ perovskite, where a PCE of more than 10% was achieved when the perovskite was adsorbed onto Al_2O_3 that was in contact with spiro-MeOTAD [25]. Al_2O_3 used in this device acted simply as a scaffold layer and not as an electron-accepting layer. Perovskites have generally been deposited in a single step onto mesoporous metal oxide films using a mixture of PbX_2 and CH_3NH_3X in a common solvent (where X is an appropriate halide). However, the uncontrolled precipitation of the perovskite produces large morphological variations causing a wide spread of photovoltaic performance in the resulting devices. Recently, Gratzel et. al. [26] have discovered a sequential deposition method for the formation of the perovskite sensitizers within the porous of the metal oxide film. PbI_2, for example, was first introduced from solution into a nanoporous TiO_2 film and subsequently transformed into the perovskite by exposing it to a solution of CH_3NH_3I.It was found that the conversion would occur within the nanoporous host as soon as the two components come into contact, permitting much better control over the perovskite morphology than previously attained. Using this technique for the fabrication of solid-state

perovskite solar cells greatly increases the reproducibility of their performance and gives a PCE of 15%.

A few authors have postulated that perovskite solar cells have the potential of exceeding the 20% PCE benchmark that needs to be crossed for a novel solar technology to be commercialized [27, 28]. Previous reports [29] have suggested a maximum current density of 28 mA/cm^2 is possible by converting photons in the range of 280−800 nm into electrons, here, 800nm corresponds to a perovskite material of around 1.5 eV band gap. If we consider 20% of light reflection occurs at the TCO glass substrate, about 22 mA/cm^2 will then become a realistic J_{sc} from a 1.5 eV band gap material device. Therefore, a PCE of around 17% (J_{sc} of 22 mA/cm$_2$, V_{oc} of 1.1 V and a fill factor of 0.7) is a realistic efficiency expectable from a $CH_3NH_3PbI_3$ perovskite solar cell with a band gap of 1.5 eV. A V_{oc} of 1.1 V is a realistic expectation after considering a driving force of 0.4 eV (0.2 eVs for electron injection and 0.2 eVs for hole extraction). In addition, if one uses a meso-superstructured structure as proposed by the Henry Snaith's group [30] where the perovskite acts as not only a light harvesting material but also as the sole electron transporting material, the photovoltage will then be determined by the difference between the Fermi energy levels of the perovskite and the HOMO level of the HTM. In this case, a photovoltage of more than 1.1 V is also possible because the only driving force to account for is the hole extraction (0.2 eV). Because a fill factor of 0.7 was already achieved, further improvement to 0.75 or more is possible by increasing the shunt resistance and decreasing the series resistance. Including antireflection or plasmonic technologies to the perovskite solar cells can only further increase the number of photons passed through the conductive substrate, which directly would improve the J_{sc} to beyond 22 mA/cm^2. For instance, reduction of the light reflection fraction from 20 to 15% by methods proposed before would lead to a J_{sc} increment to about 24 mA/cm^2. This as a result would further increase the device efficiency. There is however one drawback for this

relatively new technology, that is, its absorption range. Though it covers most of the visible region of the spectrum, it totally leaves out the near infrared regions (NIR) of the solar spectrum where a lot of solar energy exists. Hence, this solar cell is limited by its capability of absorbing solar light. This can possibly be overcome by employing NIR hole transport materials in conjugation with the perovskite materials to make more efficient solar cells.

Organic Solar Cells

Organic solar cells are photovoltaic devices that convert sun light into energy using organic (carbon containing) materials. This is unlike their inorganic or hybrid counterparts which either use a mixture of inorganic and organic materials or strictly inorganic materials such as silicon, CIGS, etc for their fabrication respectively.

Organic solar cells have been around in the research community for a long time and are progressively showing increases in their ability to convert sun light into energy (PCE) but are yet to penetrate the energy market. These solar cells, with their current PCEs (10-12%), are intended to support niche applications such as building integrated photovoltaics (BIPV) or solar bags etc. Some of the advantages they posses over their inorganic counter parts are that these devices can be easily fabricated (ink-jet printing, roll to roll coating, evaporation techniques, etc.) on flexible substrates making them light weight and easy to transport [40]. Some studies made on flexible organic solar cells have yielded some very interesting results. As can be seen in Figure 3, an ultra thin OSC was made on a polyethylene terephthalate (PET) substrate and with the help of an elastomer, the OSC's elasticity was studied. The solar cell was compressed quasi-linearly, as shown in Figure 3c from 0% compression to 30% and then 50% compression. The sample, during compression, due to reduced area available to illumination, had a decreased PCE. The interesting feature however was that the PCE was re-achieved once the cell was stretched back to its original size. This

suggests that the ultra thin solar cell can not only be folded and stored but can be re-opened and used without any drop in efficiency [35].

The other advantage OSC has is that minor chemical tuning of the organic materials makes it possible to tune the open circuit voltage (Voc) of these solar cells and also change the absorption range [39]. In order to compete with the existing solar technology and to address the international energy crisis, the efficiencies of these solar cells should approach 20%. In line with achieving this goal, the efficiencies for these devices have been increased on a regular basis. Heliatek, for example, has currently achieved 12.0% [38] efficient organic solar cells (OSCs). This information indicates that OSCs, given more time, can not only compete with conventional solar technologies but might, after a while lead them on account of their relatively cheaper means of production [40].

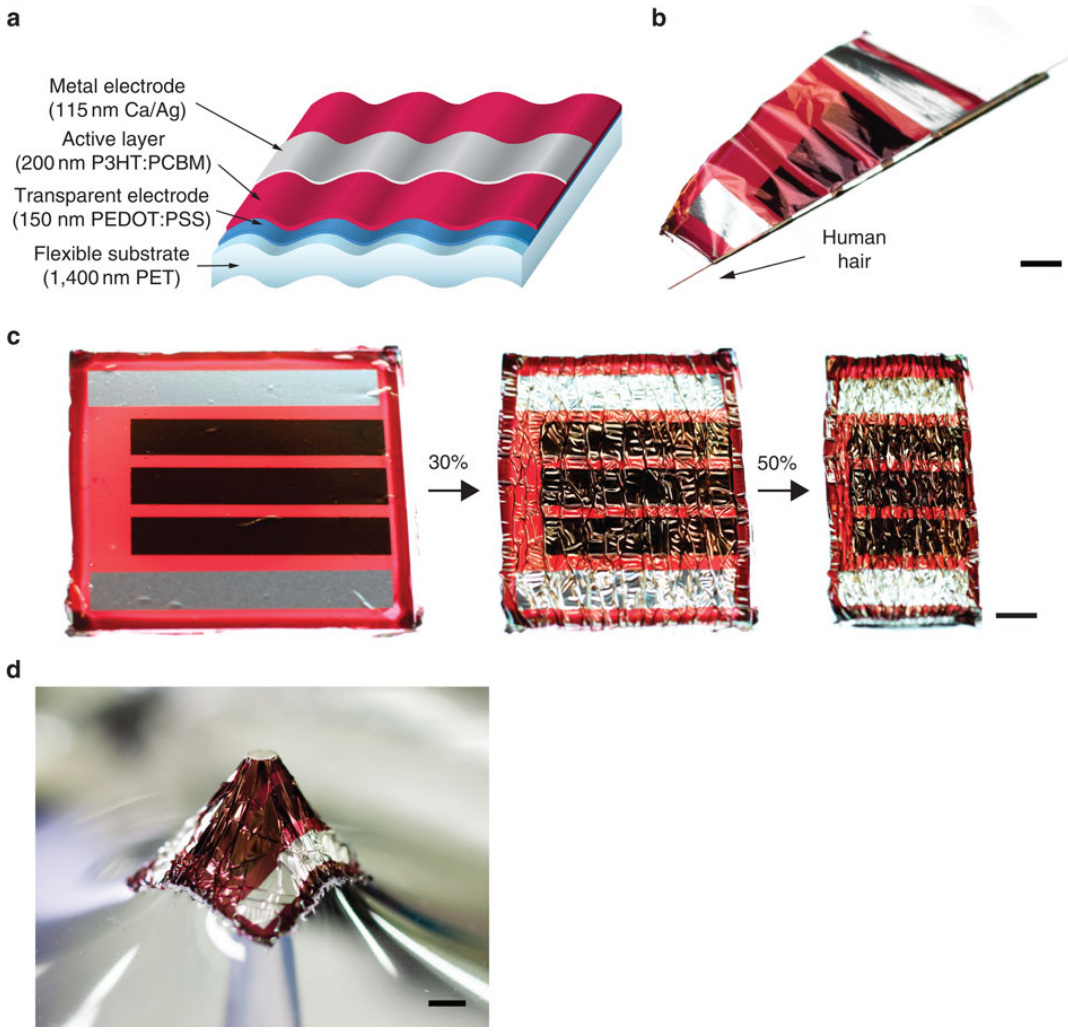

Figure 3 (a) Schematic of an ultra-light and flexible organic solar cell. The layer thicknesses are shown to scale. (b) Extreme bending flexibility was demonstrated by wrapping the solar cell around a 35-µm-radius human hair. (c) Stretchable solar cell shown flat (left) and at 30% (middle) and 50% (right) quasi-linear compression. (d) The exposed to the elastomeric support, under three-dimensional deformation by pressure from a 1.5 mm-diameter plastic tube. Adapted from [35].

Chapter 2

Literature review

Working of Organic solar cells

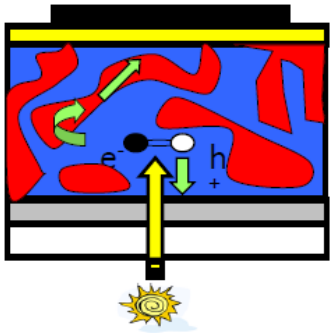

Figure 4 An artistic representation of donor and acceptor phase, charge generation and transport in an OSC.

This novel breed of solar cells, as indicated in Figure 4, is generally made of an electron donor (blue phase) and an electron acceptor (red phase). Most of the incident light is absorbed by the donor material. The absorbed light generates an exciton (bound electron-hole pairs) in the donor and this exciton travels up to the donor-acceptor interface. At this juncture, the exciton splits up giving a free electron and a hole that is then transported out of the device through the electron acceptor (acceptor phase) and electron donors (donor phase) respectively. It has been previously established that the diffusion lengths of and exiton is very short, around 10nm - 20nm [41]. Hence, it needs to be split into a free electron and hole as soon as it is generated. To assist in this, the donor and acceptor materials are inter-mixed in the bulk of the solar cell to form a bulk-heterojunction (BHJ) solar cell. This intricate intermixing of the donor and the acceptor phase in the bulk of the solar cell makes it easy for all the exitons to quickly dissociate. Consequently, the downside of such an inter-mixing is that, once the free charge is generated, it is difficult to completely extract this charge as there is no continuous donor or acceptor phase for the charges to traverse through and get extracted

from the solar cell. Therefore, an optimized nano-morphology inside the BHJ solar cell is very important to maintain a delicate balance between free charge generation and extraction.

In order to obtain a high PCE, a solar cell must be able to absorb light from the entire solar spectrum. Most of the older polymer OSCs such as P3HT and PPV based devices only covered the visible portion of the solar spectrum and hence their efficiencies have been limited to around 6.5% [42]. The newer bread of polymer solar cells made of low band gap polymers such as PTB7, PCPDTBT etc. have absorption range into the early parts of near infrared region (NIR) of the solar spectrum thereby increasing their PCEs to around 9.2% [37]. The problems, however, with polymer solar cells are that they are not very reproducible, furthermore, the polymers have a complicated synthesis process, tend to have high polydispersivity index causing batch to batch variations etc. Hence, small molecule solar cells are a better alternative in this regard.

Small molecules OSCs are traditionally prepared by vacuum deposition of the donor and acceptor materials. For this method of fabrication, metal pthalocyanines have shown decent performance (around 4%). Yet, these are not comparable to the efficiencies needed to make these solar cells commercially acceptable for large scale energy production. There are three main aspects that can be improved in this regard. Firstly, the materials base for small molecules must be improved such that more of the solar spectrum is utilized. Secondly, higher charge carrier mobility in these small molecules is essential for better solar cell performance [43–46]. Finally, like for polymer OSCs, it is essential to be able to control the morphology of the active layer in small molecule OSCs, for example by choice of solvents [47], annealing temperature [48] and concentrations of ingredients in the absorber solution [49].

Recently, solution-processed small molecule OSCs are emerging as a competitive alterative to their vacuum deposited counterparts due to their natural ease of fabrication. Furthermore, many techniques and lessons for polymer-based BHJ solar cells could be applied for small molecule BHJ OSCs [51]. Recently, prominent efficiencies (over 7%) have also been achieved for small molecule bulk heterojunction (BHJ) OSCs [50] which is closing the performance gap with the best of vacuum deposited OSCs. However, small molecule BHJ OSCs has not been investigated very intensively. It has been previously found that metal phthalocyanines have shown good solar cell performance, however, in order to fully use their chemical flexibility and to tailor the optical and electronic properties of the materials, peripheral substitution of the phthalocyanines with bulky groups or hydrocarbon chains [52-53] is essential. Those functionalized phthalocyanines show promising properties but are in turn difficult to evaporate due to their side chains [54–56]. The bulky peripheral substitutions, however, make it easier for these molecules to dissolve in organic solvents hence making it possible to deposit these materials through a solution deposition procedure there by making it easier to mass produce.

Other than the efficiency of OSCs, another serious technological problem with this bread of solar cells is their poor life time (as previously suggested). Organic absorbers generally degrade in the presence of air and light.

Improving the efficiency of OSCs

As discussed before, improving of PCEs of OSCs can not only occur due to improved absorption spectrum of the solar cells but also by better controlling the nano structure of the solar cell. This had been achieved by Ayzner et. al. [57]. They had conjured a way to prepare OSCs in a solution processed methodology but with a morphology that could compete with the more traditional bulk heterojunction fabrication method.

In this technique, Ayzner et. al. suggested that P3HT and PCBM would be coated onto an ITO glass slide one after the other by mixing them individually into ortho-dichloro benzene (*o*-DCB) and dichloro methane (DCM) respectively. The P3HT solution was first coated onto the ITO glass coated with the PEDOT:PSS and then the PCBM solution was coated on top of the P3HT layer. DCM being an orthogonal solvent to P3HT doesn't dissolve the underlying P3HT layer and as a result, a solution processed bilayer solar cell is created.

Once the solar cells were annealed and measured under one sun illumination, it was identified that the device efficiency was around 3.5% (The J-V curve for a representative device is shown in Figure 5a). This efficiency was comparable to BHJ solar cells made from the same materials combination elsewhere and in our own lab. They further presented photoluminicense (PL) results for both pure P3HT and the bilayer solution processed solar cells and suggested that the high efficiency observed for the solution processed bilayer solar cells is due to the enormous exciton quenching present in the bilayer solar cells (also shown in Figure 5b). This further led them to conclude that P3HT's exciton length has suddenly increased from 8-20 nm (as previously reported by many groups around the world) to 80 nm, a claim that rattled the scientific community.

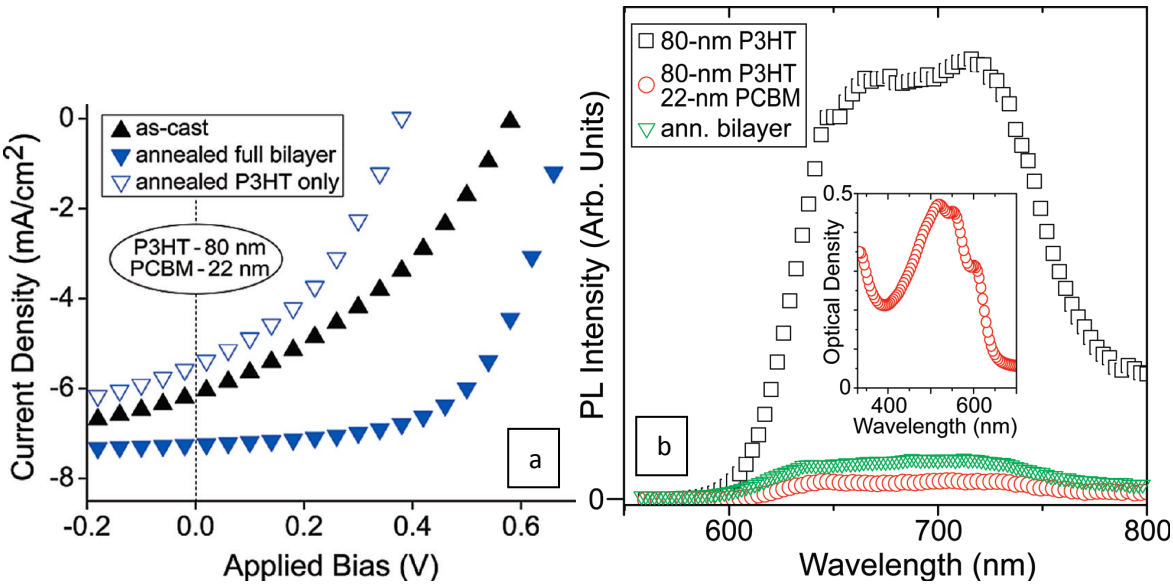

Figure 5 (a) Indicates the J-V measurement data for the solution processed bilayer solar cell when the solar cell is prepared as described before, when only the P3HT layer is annealed and when the whole bilayer is annealed. (b) PL results from bilayer OSCs and pure P3HT layer indicating the high exciton quentching capability of the new fabrication method.

This claim had also rattled out group and hence research on solution processed bilayer organic solar cells (SB-OSCs) was initiated and our main motive was to find out whether the claims made by Ayzner et. al. were correct and if not, what could explain the improved efficiency.

In our analysis, SB-OSCs were fabricated and characterized. Reports presented by Ayzner. et. al. were confirmed. In order to determine the reason behind the improved efficiency, we had singled out annealing as a deciding factor based on the solar cell's efficiency before and after annealing. Hence, three samples, one that was not annealed, one that was annealed at 140 ºC for 30 sec and one that was annealed at 140 ºC for 20 mins were first prepared. These samples were then sent for depth profiling. The results are presented in Figure 6. From this data, it was concluded that the non-annealed sample was a bilayer and the annealed sample, even the 30 sec annealed sample, was not a bilayer. This then lead to the conclusion that the improved efficiency for SB-OSCs was mainly due to PCBM's diffusion into the P3HT layer

making it into a BHJ. This explained the improved efficiency without having to change the diffusion length of excitons in P3HT [58].

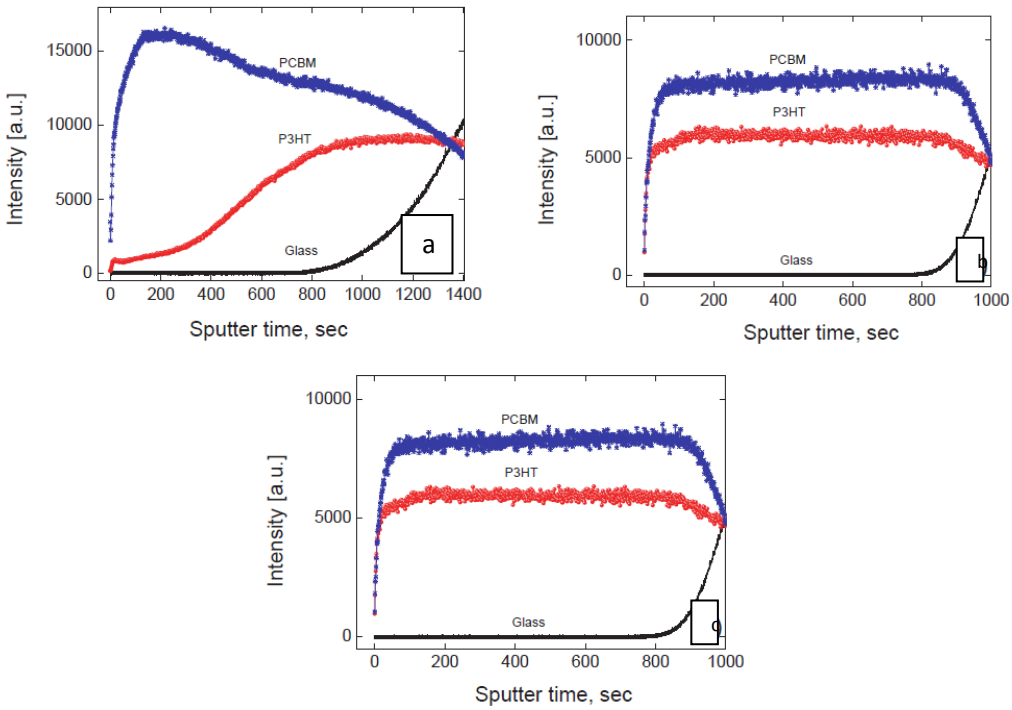

Figure 6 Shows the depth profiling done on a sample (a) non-annealed (b) 30 sec annealed sample and (c) 20 mins annealed sample. Adapted from [58]

Degradation of OSCs

Why do OSCs degrade?

Other than the efficiency of OSCs, another serious technological problem with this bread of solar cells is their poor life time (as previously suggested). Organic absorbers generally degrade in the presence of air and light.

Effect of Oxygen and Moisture on the active layer of an OSC

Oxygen and moisture are seen to diffuse into the active layer when OSCs are exposed to ambient conditions. In order to study the process and extent of this diffusion, research has be done by exposing OSCs to labeled oxygen ($^{18}O_2$) and moisture ($H_2{}^{18}O$) so as to track the progress of their diffusion through the various layers of an OSC. This has been analyzed by

conducting a time of flight-secondary ion mass spectroscopy (TOF – SIMS) analysis on the degraded samples. This TOF – SIMS experiment gives us information about the depth to which oxygen and moisture have diffused.

Through this experiment, it has been found out that oxygen and moisture mainly diffuse from the cathode and not much from the sides of the solar cell. At the cathode, oxygen and moisture enter the active layer through the pin-holes (discontinuous metal layers caused during metal evaporation) available on the metal electrode [59].

Studies had previously been done on the mechanisms of degradation for a PPV based polymers. It was found out that PPV degraded in the presence of oxygen by forming Singlet oxygen due to energy transfer from the photo-excited polymer to adsorbed ground state oxygen molecules. In order for this degradation to proceed, certain requirements are necessary: the triplet state (T_1) of the polymer must be higher in energy than the singlet state of oxygen for the energy exchange to take place. The intersystem crossing from the polymer S_1 to T_1 states must also be reasonably favored and the T_1 state has to be in existence for long enough time to enhance the probability of the energy exchange. Then, the singlet oxygen is believed to react with the vinylene groups in PPVs through a 2+2 cyclo addition reaction. The intermediate adduct might then break down resulting in chain scission [60].

In other work, devices made from P3HT and PCBM were used to study the effect of continued exposure of moisture and oxygen and its effects on the device performance. It was found out that the effect of oxygen was permanent and the effect that moisture has on the solar cell is more reversible. An experiment was done by varying the amount of moisture in pure nitrogen atmosphere from less than 1% relative humidity (RH) to around 40% RH. It was found that the exposing the solar cell to moisture had indeed reduced the fill factor (FF), short circuit density (J_{sc}) and open circuit voltage (V_{oc}). The effect it had on the J_{sc} and FF

was very small and was relatively independent of changes in the relative humidity but the effect on V_{oc} was more significant. The reason for this observation is probably due to changes in transport properties of the PEDOT: PSS-active layer interface. When a change in voltage is observed, it is most often due to a change in the band edges for the materials at the interface. Possible mechanisms that could account for this observation are a reorganization of molecules at the interface that lead to a change in the effective work function of PEDOT:PSS by affecting either the carrier density in PEDOT:PSS near the interface or the formation of a dipole layer at the interface or both. It has been seen that heating the sample causes it to regain most of its lost performance [61].

Electronic identification of degradation

Like PPV, P3HT also reacts with oxygen to form a charge transfer complex resulting in p-doping of P3HT. This has also been investigated theoretically by band-structure calculations. Furthermore, oxygen induced degradation of P3HT is reported to result in decreased mobility and increased trap densities. Similar finds hold for C60 exposed to oxygen as well. This was demonstrated by investigations of C60 based field effect transistors. The important issue here is the electronic effect degradation has on the solar cell. It is clear from this discussion that degradation electronically manifests itself as trap-states and therefore, a measure of the number of trap-states present in a solar cell is indicative of the extent to which the solar cell has been degraded [62].

Thermally Stimulated Current

One of the traditional techniques to identify and estimate trap-states in OSCs is thermally stimulated current (TSC).

This technique works by cooling the sample to close to absolute zero (~10 K) and then illuminating the sample. This way, the organic solar cell, at the previously prescribed low

temperature has photo generation occurring in it and once free electrons and holes are created in the sample, they tend to move out of the sample. Since the donor and acceptor material already has trap-states, these charges tend to fall into those trap-states. For charges to get out of these potential wells (trap-states), thermal excitation is needed and since the sample is cooled down to around 10 K, this option is unavailable. Therefore, the electrons and holes cannot be thermally excited out of the potential wells and hence are trapped there. Now, the charges have a few options:

(a) Since 10 K is still above 0 K, some charges might still get excited out of the trap-states and removed the device or recombine once they get de-trapped (excited out of the trap-staes).

(b) These charges inside the trap-states can undergo trap-assisted recombination, meaning, trapped-electrons recombine with trapped-holes or trapped electrons recombine with free holes or trapped holes recombine with free electrons.

The above elucidated procedures are possible ways of loosing electrons and holes before they can be extracted out of the device.

Next in the procedure of TSC is that the sample will then be slowly heated at around 10 K/min. This way, the OSC sample is gaining more thermal energy meaning that more electrons and holes that are trapped have enough thermal energy (shallow trapped charges – low energy trap-states) to get de-trapped and extracted out of the solar cell. This way, like explained before, there are many loss mechanisms by which charges can be lost but charges will also be extracted out of the device.

Now, this procedure of gradual heating is continued along with recording the current at various temperatures. The total number of charges extracted out of the device by this extraction procedure is recorded and against each temperature and a plot is made. This plot

then gives us a lower estimate (since there are many charge loss mechanisms involved) of the total number of charges at each trap-depth.

Figure 7 shows a picture of the data obtained from a TSC measurement made on a P3HT and P3HT:PCBM sample. Here, to gain a deeper understanding of the underlying degradation mechanisms in P3HT:PCBM solar cells, the author had performed TSC measurements to obtain information about the electronic trap-states for dark as well as photo-degradation. First of all, the trap distribution of non-degraded P3HT:PCBM solar cells was investigated by applying a TSC measurement on it. The resulting density of occupied states (DOOS) distribution (number of trap-states vs energy depth) is shown in Figure 7. The activation energies (thermal energy need by a charge to de-trap) of the traps range from 20 to 400 meV with the centre of distribution at about 105 meV. For further interpretation of the DOOS distribution of the blend, the authors had considered the results from a pure P3HT sample (results also shown in Figure 7). For P3HT, the DOOS was related to two different overlapping traps with approximately Gaussian energy distributions, with the centre of distribution of the dominant trap at about 105 meV (T_2) and the other at about 50 meV (T_1). Since the centres of distribution for the blend as well as the pure P3HT are at 105 meV, they attributed the dominant traps in the solar cell to have come from P3HT, although the distribution of the main trap in the blend is broadened as compared to the pure P3HT,

indicating a higher disorder in the blend [62].

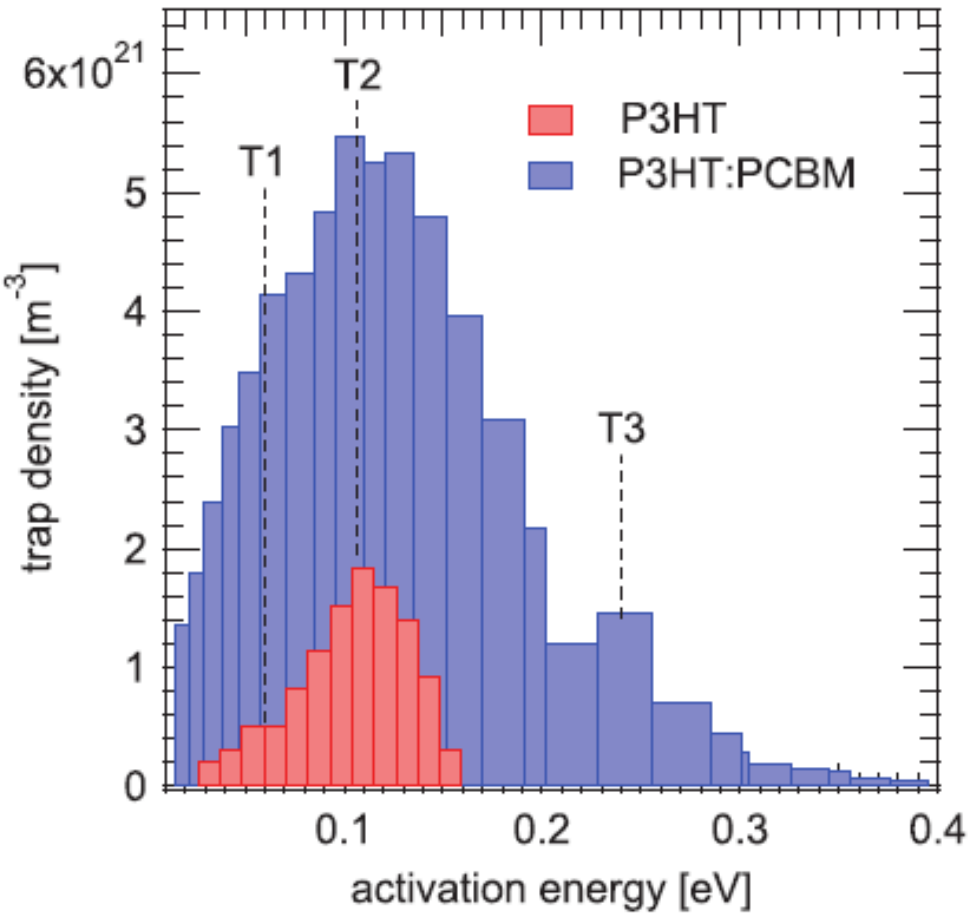

Figure 7 Depicts a lower estimate of the total number of trap-states present in P3HT and P3HT:PCBM samples at various energy depths as predicted by a TSC measurement [60].

Chapter 3

Experimental Procedures and Instrumentation

Discussed in this chapter of the thesis are the materials used and the experimental procedures used to fabricate the solar cells and the conditions used to obtain degraded solar cells. Apart from that, a brief discussion of how each of the equipment works is also illustrated in this chapter.

Materials

The materials used in the investigation were as follows: Regio-regular (≥ 98%) poly(3-hexylthiophene) (P3HT) was purchased from Sigma Aldrich. Poly(3,4-ethylenedioxythiophene):poly(styrene sulfonate) (PEDOT:PSS) was purchased from Ossila limited. Phenyl-C61-butyric acid methylester (PCBM), was purchased from Nano-c. Indene-C60 bisadduct (ICBA) was purchased from Luminescence Technology Corporation (product code LT-9030). All the solvents that were used in the present investigation were purchased from Sigma-Aldrich. Aluminium (Al) was purchased from STREM chemicals Inc. and Calcium (Ca) was purchased from K.J.Kurt Lesker & Co. All the above mentioned materials were used as received.

Experimental Procedures

Solar cells are fabricated on top of a glass coated with transparent conducting oxide (TCO). ITOs were used in our case. Before this procedure is carried out, there are a few steps that are conducted to achieve working solar cells, they are:

1. ITO cleaning
2. PEDOT:PSS coating
3. Solution preparation
4. Sample preparation inside the glovebox
5. Sample exposure

6. Cathode deposition

Each of the above five process will now be briefly discussed below:

ITO Cleaning

Pre-patterned Indium tin oxide (ITO from XINYAN TECHNOLOGY LTD) substrates were first obtained. The sheet resistance of the ITOs was around 15-20 Ω per square. Then, firstly, the ITO substrates were thoroughly manually cleaned using a detergent solution under flowing tap water. Then, the ITO substrates were successively sonicated in deionised water first, acetone next and finally in isopropanol. Each of the sonication step was conducted for 15 min and the substrates were then dried in an oven for 3 hours. This process gets rid of any organic or inorganic waste that was present on the ITO substrates. This step was then followed by a UV-ozone treatment for 15 minutes. The UV ozone treatment makes the surface of the ITO very hydrophilic thereby preparing the ITO substrate for the subsequent processing step.

Here, in Figure 8a, the gray portions represent ITO on the underlying glass substrate. This pattern is deposited by the company from which the ITO slides are procured. The four ITO pads on either sides of the long ITO strip in the centre are used to provide better metal contacts once the cathode is deposited.

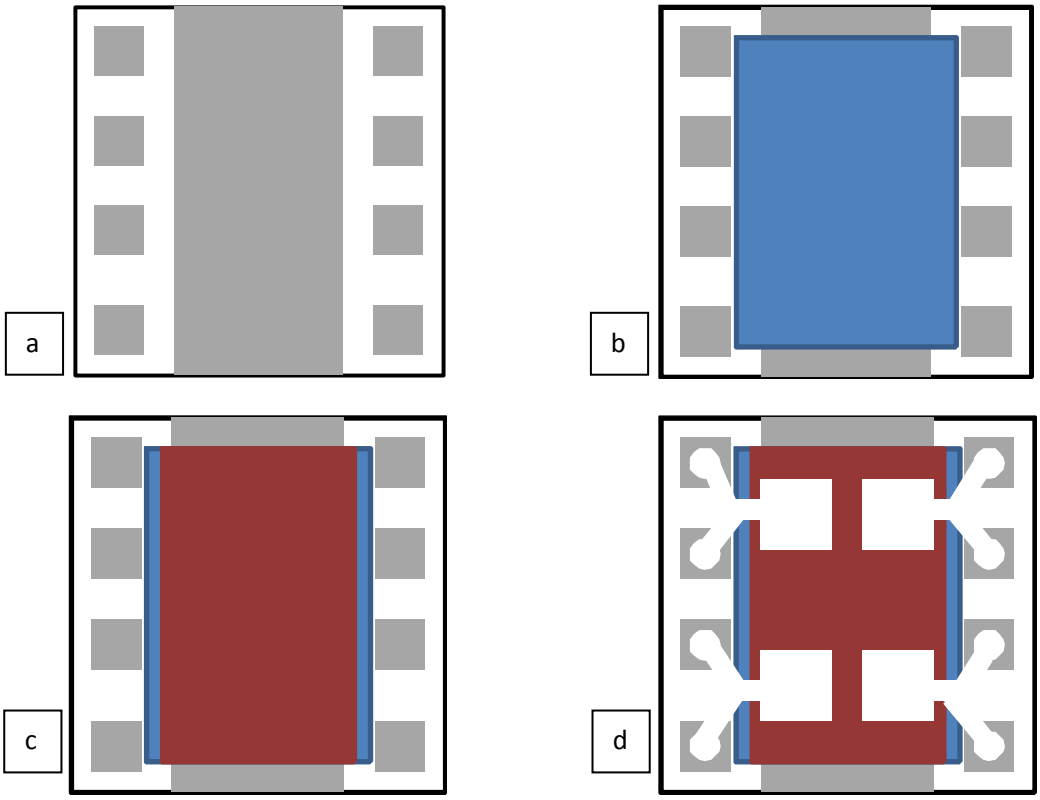

Figure 8 (a) Cleaned ITO pattenered substrate. The four squares on either sides are called ITO pads and are used to provide a more robhust metal contact. This will be later explained. (b) Shows an ITO slide that has been coated with a layer of the hole selective layer of PEDOT:PSS. Apart from that, its edges are also wiped clean allowing a better cotnact between the counter electrode and the ITO pads. (c) Sample's schematic after the organic semiconducting layer is deposited and edge removed (d) A topside view of the sample once the cathodes are deposited. It can be seen here that the ITO pads at both the sides of the sample are used to reinforce the contact with the counter electrode.

PEDOT:PSS coating

After the ITO substrates were cleaned and UV-ozoned, a cold solution of PEDOT:PSS was then spin-coated onto the ITO substrate. The solution of PEDOT:PSS is a water based solution and hence the UV-Ozone treatment of the substrate is essential for the PEDOT:PSS to form a layer on top of the ITO substrate. Once a layer is formed, the edges are wiped clean with a tissue paper soaked in plain water to help gain a proper contact later when the metal contacts are evaporated. A schematic of the ITO slide after the PEDOT:PSS layer deposition and edge cleaning is shown in Figure 8b.

Solution preparation

Bulk heterojunction solar cell's solution preparation (BHJ)

A blend of our organic sensitizer, a mixture of the donor and the acceptor materials is prepared by mixing a P3HT and PCBM in a common solvent, ortho-dichlorobenzene (*o*-DCB). The solution is prepared inside an inert glovebox (Oxygen < 5 ppm, H_2O < 1 ppm) such that the P3HT:PCBM weight ratio is about 1:0.8 and the P3HT concentration is around 15 mg/mL. Once the solution is prepared, it is left to stir overnight (14-16 hrs) inside the glovebox at around 60 ºC.

Pseudo bilayer organic solar cell's solution preparation (PBL)

A solution of P3HT is first prepared in an *o*-DCB solvent at a concentration of 15 mg/mL. The solution is then left stirring overnight at 60 ºC. *o*-DCB, being a high boiling point solvent, the solvent didn't evaporate easily and hence the solution's concentration did not change much overnight.

Next, a solution of PCBM/ICBA is made by dissolving PCBM/ICBA in a solvent of dichloro methane (DCM). DCM being a highly volatile solvent is mixed with PCBM/ICBA about 1 hr before the solution is used. The PCBM/ICBA concentration used here is 7.4 mg/mL.

Sample preparation inside the Glovebox

The PEDOT:PSS coated samples are left in a vacuum ante-chamber over night (~14-16 hrs) before they are brought into a glovebox (Oxygen < 5 ppm, H_2O < 1 ppm). Once inside the glovebox, the samples are annealed at 140 ºC for about 20 minutes. The samples are then immediately cooled off to room temperature.

After the samples are cooled, they are coated either to form BHJ or PBL organic solar cells.

BHJ solar cells

In order to make these solar cells, the cooled sample was coated with the BHJ solution. The solution is filled into a syringe and released onto the sample through a 450 micron PTFE filter. With this, a 180 nm – 200 nm layer of the blend is then coated onto the sample with the help of a build in spin coater.

PBL solar cells

In this case, first a layer of P3HT is coated onto the cooled sample. The pure P3HT solution is first passed through a 450 micron PTFE filter and dropped onto the sample. The spin coater is then used to coat an 80 – 100 nm thick layer of P3HT. The PCBM/ICBA solution (in solvent DCM) is then dropped onto the pre-coated P3HT layer through a micro-pipette. Since DCM is an orthogonal solvent to P3HT (meaning, it doesn't dissolve P3HT), a layer of PCBM/ICBA is coated on top of the P3HT by spin-coating. As a result, a layer of 20 nm thick layer of PCBM/ICBA is coated on top of the pre-existing P3HT layer. Once this is done, the sample is once again annealed at 140 ºC for about 20 minutes.

In both the sample preparations, the edges of the sample are cleaned with the help of a cotton swab dipped in *o*-DCB. This helps with better contact with once the cathode is deposited. A schematic of the sample at this stage is shown in Figure 8c

Now, samples are ready for exposure.

Sample exposure

This fabrication step only applies to those devices that need to undergo controlled degradation.

In the event that a sample needs to be degraded in a controlled manner, the samples, after the organic layer deposition, is removed from the glovebox and exposed to the ambient

conditions for a specified amount of time. The longer the exposure, the more the sample degrades. Once the stipulated time of degradation is completed, the samples are transferred into another glovebox where electrode deposition is carried out.

Cathode deposition

Once the samples are transferred into the thermal evaporation glovebox, they are loaded into a substrate holder and are placed under an evaporation mask (to get the intended cathode pattern with the intended dimensions). This sample holder is then loaded into a high vacuum chamber and pumped down to a pressure of around 4×10^{-6} mBar. The samples then undergo evaporation process where lithium floride (LiF) and aluminium (Al) is melted and evaporated one after the other in the same order to form an electron selective layer and a cathode respectively. The pattern deposited on the sample can be understood by looking at Figure 8d. This evaporation helps us define the active solar cell area at around 0.09 cm^2. Apart from that, from Figure 8d, it becomes evident that the ITO pads on the sample's extreme right and left are there to help us make reinforced contacts with the cathode.

Instrumentation

The various instruments used in the course of this thesis are listed below:

1. Time of flight – Secondary ion mass spectroscopy (TOF-SIMS)
2. Current-voltage measurements
3. Photoluminescence measurements
4. Photo – CELIV
5. External quantum efficiency
6. Absorption measurements

Time of flight – Secondary ion mass spectroscopy (TOF-SIMS)

TOF – SIMS is used to determine the thickness profile of an organic layer. This technique gives us the concentration of either P3HT or PCBM as a function of the depth of the device. P3HT and ICBA layers were spin coated onto a glass substrate in a fashion similar to that of the solar cell fabrication for the TOF-SIMS measurements. Sulphur is used as the marker for P3HT. Since the PEDOT:PSS layer also contains sulphur , a smooth bare glass substrate (with RMS roughness less than 1nm) was used instead of the Glass/ITO/PEDOT:PSS substrate. For the TOF-SIMS measurements, 25 KeV Bi_3^+ analysis gun with a 0.8 pA current was used to analyse the layer. The dimension of the sample area under analysis was 100 µm x 100 µm. A 0.5 KeV Cs^+ sputtering gun with a 40 nA current was used to etch away a layer of dimension 300µm x 300µm to facilitate depth profiling.

Current-voltage measurements

The current-voltage (i–V) measurement is a fairly common way of evaluating the performance of a solar cell. The i-V curves measured for in this work were subject to 1 sun illumination from a sun simulator. The intensity was calibrated using a silicon reference cell (Fraunhofer ISE). Measurements were corrected by applying a spectral mismatch factor. The resulting efficiency values were also confirmed from the SERIS calibration laboratory [63].

Photoluminescence measurements

Photoluminescence (PL) measurements are also a fairly common mode of characterizing solar cells. PL measurements were made to determine the extent of exciton dissociation in organic solar cells. In our setup, Avantis 2048 spectrometer and a Labsphere integrating sphere was used. The excitation source for the PL measurements was a 25 mW Nd:YAG laser operated at a wavelength of 532 nm. All the fabrication steps after the deposition of PEDOT:PSS layer onto the ITO substrate and characterisations were performed inside the glovebox under nitrogen atmosphere.

Photo – CELIV

This technique was used to obtain the charge carrier mobility inside a working solar cell. The photo – CELIV setup used for this experiment comprises of an oscilloscope (Lecroy WaveJet 354A), a voltage function generator (Agilent 33522A) and a LASER source (531 nm, nano second pulsed LASER, STANDA, STA-01SH-03). The solar cell was then connected in series to the oscilloscope and later to the function generator.

External quantum efficiency (EQE)

EQE measurements were made by measuring the short-circuit current density under monochromatic light for the test device and a reference calibrated photodiode (Calibrated at Fraunhofer ISE). The monochromatic light was supplied by a xenon lamp coupled to a monochromator. The light from the monochromator was passed through a chopper with a chopping frequency of 300 Hz. This was done to isolate the photoelectric current response of the solar cell by the monochromator from the response that comes from the ambient light. The data was collected by custom developed EQE software. All measurements were made in a nitrogen glovebox.

Absorption measurements

A transmission absorption measurement was made here and this was done by using a halogen lamp as light source, Labsphere's integrating sphere and an Avantis 2048 spectrometer. The light was first passed through a plain ITO coated glass slide and the spectrometer's response was recorded (Curve1) using third party software (Avasoft). Next, a sample with an organic material coated was used to block the light coming from the halogen lamp. The transmitted light was again recorded with the help of Avasoft (Curve2). The absorption spectrum of the curve was then obtained by following the following equation:

Absorption (%) = $\left(\frac{Curve1 - Curve2}{Curve1}\right) \times 100$

Chapter 4

Results and Discussion

Prelude to current research work

My work has been focused in achieving both higher efficiency and to identify degradation caused trap-states. The later is important as it can be used as a technique to identify methods that cause or prevent degradation in OSCs.

P3HT:ICBA bilayer solar cells

In order to first tackle the efficiency issue plaguing OSCs, work presented here focuses upon fabricating bi-layer organic solar cells using sequential processing technique using ICBA as electron acceptor and P3HT as electron donor. The PCE of P3HT:PCBM, as explained before, is limited due to the following factors a) limited light harvesting by the polymer P3HT due to a relatively high band gap (~1.9 eV) and b) lower open circuit voltage of approximately 0.6 V that is attributed to the small energy difference between the highest occupied molecular orbital (HOMO) of P3HT and the lowest unoccupied molecular orbital (LUMO) of PCBM [64]. A novel indene-C60 bisadduct (ICBA), introduced before, was synthesised recently by Li et al. with a higher LUMO energy level of −3.91eV which is 0.17 eV higher than that of PCBM and was used in fabricating solar cells based on P3HT as donor material. These solar cells have shown a high V_{OC} of 0.84 V [65]. The effectiveness of ICBA, used to make bilayer OSCs has been investigated in this work. Even though the devices were prepared by sequential processing technique using orthogonal solvents, a strong inter-mixing of the active components was observed due to the inter-diffusion of the ICBA into the P3HT layer by thermal annealing, thus resulting in a device close to that of a BHJ configuration. This is not very different to what was observed in the case of P3HT:PCBM SB-OSCs (also called pseudo bilayer OSCs due to its quick intermixing). The inter-diffusion process and the morphology evolution of these pseudo-bi-layer P3HT: ICBA

cells were studied using Time of Flight - Secondary Ion Mass Spectrometry (TOF-SIMS) depth profiling measurements. Various thermal annealing treatments were undertaken to study the morphology evolution of these devices and charge carrier mobility measurements through photo-CELIV technique was further used to see the effect of thermal annealing on these devices. These tests were useful in identifying the reason for the improved efficiency achieved due to annealing.

The pseudo bilayer solar cells made from P3HT and ICBA were fabricated using the fabrication steps previously described in the experimental part of the thesis. Once samples are prepared in that manner, the following tests are conducted on them.

Effect of thermal annealing - time and temperature

This test was performed to determine the extent to which thermal annealing effects the performance of the pseudo bilayer OSC. Thermal annealing is a common technique used to improve the performance of an organic solar cell [66, 67]. It is believed that the thermal annealing treatment imparts higher crystallinity and renders more ordered intra-chain interactions in the polymer P3HT [48] and also improves the crystallinity of the acceptor fullerene [68]. The evolved nanomorphology of P3HT/ICBA bi-layer films through various annealing temperatures and annealing time has significant impact on the photovoltaic properties. Typical photovoltaic parameters and current density-voltage curves are presented in Figure 10a, c-e whereas detailed photovoltaic data, collected for the individual devices are listed in Table 1.

From previous experience in fabricating P3HT:PCBM based pseudo bi-layer organic solar cell it was realized that thermal annealing at 140°C for a definite amount of time is necessary for better performing solar cells [58]. The molecular structure of ICBA (Figure 9a) is similar to that of PCBM (Figure 9b) with both possessing identical C60 bucky ball backbone except

that ICBA has a indene side chain whereas PCBM has a butyric acid methyl ester side chain and hence it was assumed that the inter diffusion mechanism and crystallisation process might be similar in both the cases. Keeping this in mind several identical solar cells were fabricated applying different annealing temperatures and annealing times. The results presented below in Table 1 are from three sets of samples. First set of samples were of devices that were annealed by keeping the annealing temperature constant at 140°C but varying the annealing time from 30 seconds to 20 minutes.

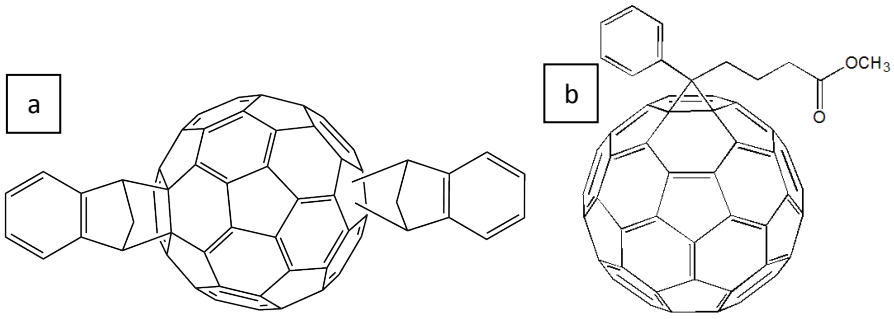

Figure 9 Chemical structures of (a) ICBA and (b) PCBM.

Table 1 Photovoltaic parameters of the P3HT:ICBA organic solar cells studied under different annealing conditions (jSC: short circuit current density, VOC: open circuit voltage, FF: fill factor). Device structure for the pseudo-bi-layer solar cells: ITO/PEDOT: PSS/P3HT/ICBA/Ca/Al. The active area of all the cells was 0.09cm^2.

Annealing time [minutes]	Voc [V]	jsc [mA/cm2]	FF [%]	Efficiency [%] (+/- 0.2%)
Batch A annealed at 140°C				
0	0.79	6.2	42.5	2.1
0.5	0.82	6.3	40.9	2.1
2	0.83	7.4	45.5	2.8
6	0.83	8.3	52.9	3.7
8	0.83	8.1	58.5	4.0

10	**0.83**	**8.1**	**57.9**	**3.9**
12	**0.82**	**8.1**	**60.7**	**4.1**
20	**0.82**	**8.3**	**62.9**	**4.3**
Batch B annealed at 140^{o}C				
20	**0.85**	**8.9**	**58.3**	**4.4**
30	**0.84**	**8.6**	**59.1**	**4.3**
40	**0.85**	**8.9**	**60.8**	**4.6**
50	**0.85**	**9.6**	**69.3**	**5.6**
60	**0.84**	**9.1**	**67.7**	**5.2**
Batch C annealed at 150^{o}C				
5	**0.86**	**7.7**	**47.8**	**3.2**
10	**0.86**	**8.8**	**67.2**	**5.1**
15	**0.85**	**8.8**	**67.7**	**5.1**
20	**0.85**	**8.7**	**72.2**	**5.4**
25	**0.85**	**8.7**	**72.8**	**5.3**
30	**0.85**	**8.9**	**68.6**	**5.2**

In the case of P3HT:PCBM bi-layer organic solar cells, it has been proven that an annealing time of 30 seconds is more than enough to achieve an optimum device performance [58]. However, in the case of P3HT:ICBA bi-layer organic solar cells, a similar observation was not made. Instead, as can be observed from Figure 10a the efficiency of the devices keeps increasing from 2.1% for the non-annealed sample and 30 seconds annealed sample to respectable 4.3% for a 20 minute annealed sample and this increase is attributed to the improvement in the short circuit current density and fill factor. The exciton dissociation at the

P3HT/ICBA interface is very efficient for both the non-annealed and annealed samples as indicated by the photoluminescence (PL) measurements (Figure 10b). The efficient charge separation between the donor and acceptor for both the non-annealed sample and the annealed samples can be seen from the quenching (~80-85%) of the intense PL peaks observed around 650 nm and 700 nm in the PL spectrum of the pristine P3HT film (Figure 10b). As the exciton diffusion length is generally less than 10nm [73, 74] inside the P3HT phase, the present findings lead to the inference that the ICBA is already partially or completely intermixed with the P3HT even without thermal annealing. Hence, we can conclude that the non – annealed sample is no longer a perfect bi-layer. It is known from other reports also that dichloromethane is not a completely orthogonal solvent for P3HT and hence during the spin coating of ICBA onto the P3HT layer, DCM dissolves the P3HT partially causing partial inter-mixing [58, 69, 70]. The extent of diffusion can be identified through TOF – SIMS analysis (described later).

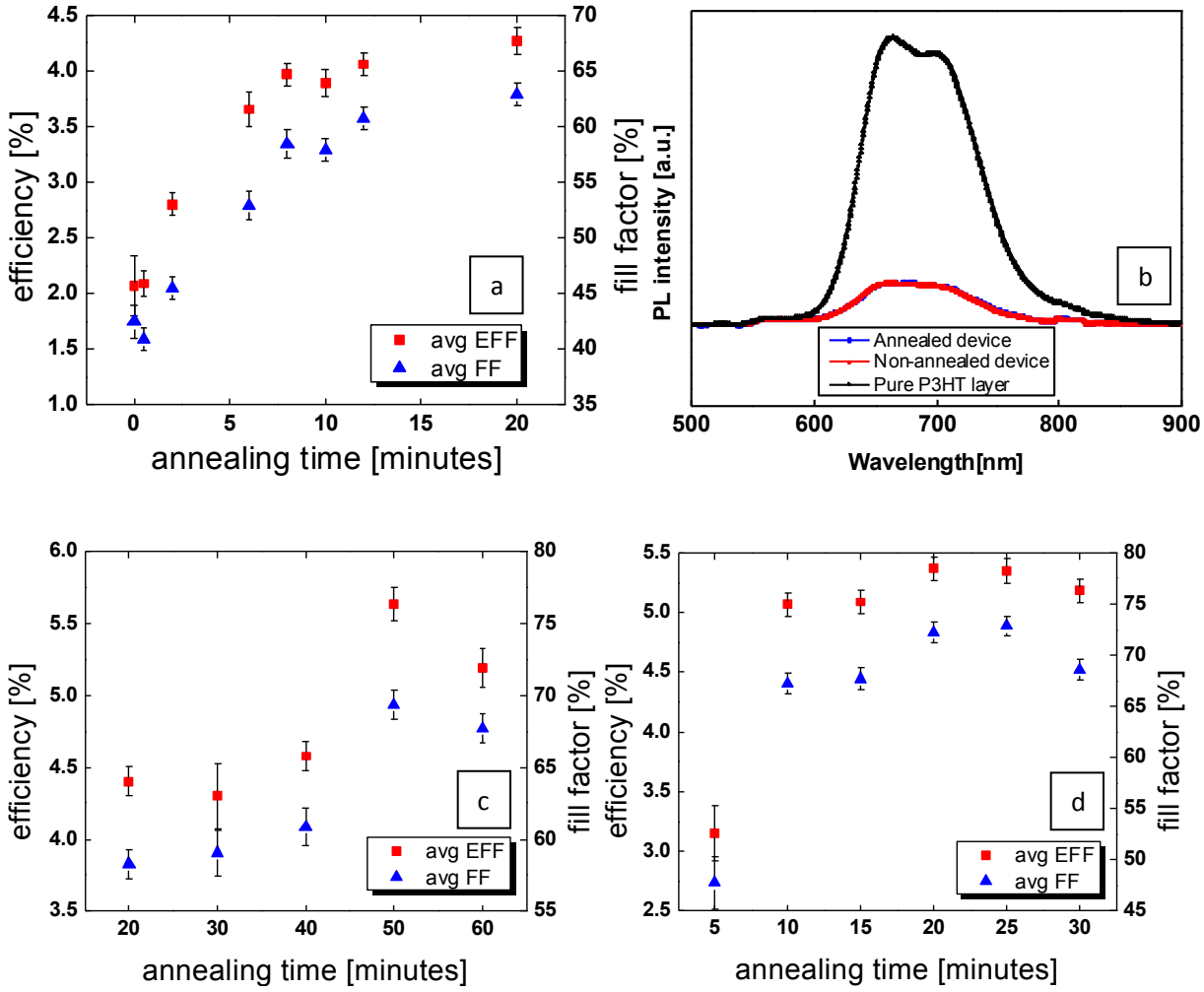
efficiency [%]
fill factor [%]
annealing time [minutes]
a
avg EFF
avg FF
PL intensity [a.u.]
Wavelength[nm]
b
Annealed device
Non-annealed device
Pure P3HT layer
c
d

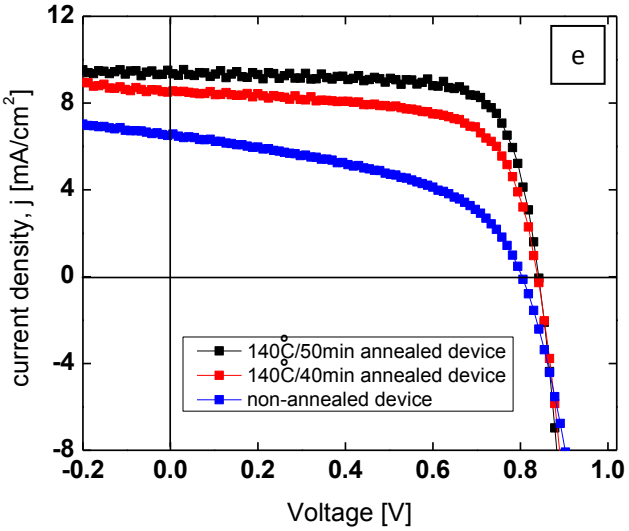

Figure 10 (a) Efficiency (EFF) values averaged over three solar cell samples are shown for different annealing times with a fixed annealing temperature of 140°C. Close to room temperature (25°C), the efficiency of the non-annealed sample was found to be 2.1% and at 30 seconds, 2 minutes, 6minutes, 8 minutes, 10minutes, 12 minutes and 20 minutes (annealing at 140°c) the efficiency was found to be 2.1%, 2.8%, 3.7%, 4.0%, 3.9%, 4.1% and 4.3% respectively. The efficiency doesn't seem to saturate around 140°C (b) Photoluminescence (PL) spectrum of the pure P3HT film and the annealed and non-annealed pseudo-bilayer solar cell (excitation wavelength 532 nm) are shown here. Both pseudo-bilayer devices show very similar PL quenching efficiency (~ 85%) which indicates that the exciton dissociation is very efficient even at partial phase intermixing conditions (c) Efficiency values averaged over three solar cell samples are shown for different annealing times with a fixed annealing temperature of 140°C. The efficiency of the 20 minute annealed sample was found to be 4.4% and at 30 minutes, 40 minutes, 50minutes and 60 minutes (annealing at 140°c) the efficiency was found to be 4.3%, 4.6%, 5.6% and 5.2% respectively (d) Efficiency values averaged over three solar cell samples are shown for different annealing times with a fixed annealing temperature of 150°C. The efficiency of the 5 minute annealed was found to be 3.2% and at 10 minutes, 15 minutes, 20minutes, 25 minutes and 30 minutes (annealing at 150°c) the efficiency was found to be 5.1%, 5.1%, 5.4%, 5.3% and 5.2% respectively (e) j-V curve of the annealed and non-annealed pseudo-bilayer solar cells at 1 sun illumination. The imperfect acceptor crystallinity for the non-annealed device leads to poor charge carrier extraction and in turn low fill factors (FFs).

It is known that different fullerenes respond differently to thermal annealing and ICBA in particular needs higher temperature for better crystallinity [65, 68]. As the power conversion efficiency seems not to saturate with a thermal annealing of 20 minutes at 140°C (Figure 10a) we fabricated another two sets of devices a) varied the annealing times from 20 minutes to 60 minutes and kept the annealing temperature constant (140°C) b) devices were annealed at 150°C for a shorter period of time - 5 to 30 minutes. Results from the above set of experiments indicate that an annealing time of 20 minutes is optimum for an annealing temperature of 150°C whereas an annealing time of 50 minutes is required for 140°C after

which the efficiency drops in both the cases (Figure 10d, c). The latter device performed marginally better (5.6%) than the former device which showed an efficiency of 5.4%. It can thus be concluded that lower annealing temperature (140°C) would need longer annealing time whereas higher annealing temperature (150°C) would need lower annealing times. The champion cell had an open circuit voltage of 850 mV, short circuit current density of 9.4 mA/cm^2 and a fill factor of 73.7 % leading to a remarkable efficiency of 5.9%. It is worth reminding here that we fabricate several identical devices and the average efficiency for 50 minutes annealed sample at 140°C was found to be around 5.6 % (± 0.2%).

It is interesting to note from Table 1 that the increase in power conversion efficiency is predominantly due to the concomitant increase in the short circuit current density and fill factor for the thermally annealed devices. The open circuit voltage was found to be not affected with annealing times among the same batch (± 10mV). As shown in Figure 10e, longer the annealing time, better is the device fill factor and hence, better is the charge transport. Thermal annealing increases the crystallinity of fullerene which helps in reducing the structural disorder that is present in the non-annealed device as the inherent morphology of the fullerene layer is amorphous in nature when spin coated from solvent like DCM which has a very low boiling point and this results in a large degree of structural disorder and imparts relatively poor electron mobility. Thermal annealing gives rise to enhanced nanomorphology and helps in better connectivity of the donor and acceptor phases that originate from the diffusion of ICBA from the top layer into the bottom layer in the vertical direction (Scheme). A good nanomorphology is vital for a good working organic solar cell as it has direct influence on the exciton generation and transfer, dissociation and charge separation, charge transport and collection at the electrodes [71, 72]. The morphology arising from this fabrication method seems to lead to a better phase separation between the acceptor and donor phases which lead to a good balance between the charge carrier generation and

extraction, whereas the non-optimal morphology of the bulk heterojunction leads to a high series resistance and low fill factor. The optimised BHJ has an open circuit voltage of 820 mV, short circuit current density of 9.4 mA/cm^2 and a fill factor of 66.3 % leading to an efficiency of 5.1%.

External Quantum Efficiency measurements

External quantum efficiency (EQE) of a solar cell was the next test employed to understand the effect that annealing a sample has on pseudo bilayer P3HT:ICBA bilayer solar cell. It is generally a combination of the extent of absorption, the effectiveness of charge separation and the extent of charge extraction. Figure 11 shows the EQE of both the annealed and the non - annealed samples. A lower EQE was observed (around 35%) for the non – annealed sample whereas an EQE of around 60% was observed for the annealed sample. The lower EQE of the non-annealed sample can be attributed to bad absorption, bad charge separation or bad charge extraction. A better EQE and an improved j_{sc} are seen for the optimally thermal annealed samples. This can be understood from the process of photocurrent generation. To obtain higher photocurrent, strong and broad absorption of the active layer is required. There is no appreciable difference in the UV-vis absorption spectra for the annealed and the non-annealed sample and the absorption peak of the non-annealed sample show marginally lower absorptance than the annealed sample (both the films are formed under the same conditions) [58]. Thus, other factors, such as charge separation and charge transport should be taken into account for the observed improvement in the j_{sc}. The absorption measured for an annealed and a non – annealed sample were similar and the photoluminescence (PL) for both the samples yielded similar quenching efficiencies (of around 85%, shown in Figure 10b). Therefore, the presence of

similar absorption and quenching efficiency suggest the possibility of bad carrier extraction in the non-annealed device as being a key reason for a lower EQE and a lower efficiency. Bad charge carrier extraction encompasses the various loss mechanisms present in the device, namely bimolecular recombination, trapping of charges and trap assisted recombination etc. These loss mechanisms result in a poor charge transport [75-78].

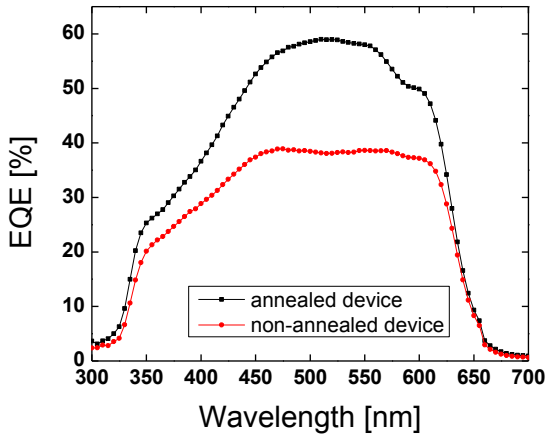

Figure 11 EQE of annealed and non-annealed device. Both the devices show a shoulder at around 600 nm corresponding to the crystallinity of P3HT

Photo – CELIV measurements

Charge carrier mobility measurements of the devices were performed next to identify the effect that annealing was having on the charge transport properties. The mobility was obtained using photo-CELIV (charge extraction by a linearly increasing voltage) technique. A difference in device parameters such as fill factor, efficiency and EQE suggested that the charge transport in the annealed and non-annealed devices might be different. A non-annealed device and an annealed device (annealing done at 140 ºC for 50 min) were encapsulated with an epoxy inside the glove box and were then tested at ambient conditions. Charge carrier extraction for the non-annealed and the annealed samples were carried out with a linearly increasing voltage pulse with a pulse width of 20 µs and a maximum voltage

of 2.5 V. The results are shown in Figure 12. From the figure and with the help of the equation below, an estimate of the charge carrier mobility for the non-annealed and the annealed samples can be made [79]. (For definition of the parameters see Figure 12)

Equation 1 Parametric equation used to obtain the mobility of charge in an OSC from raw data obtained from a Photo - CELIV result.

$$\mu = \frac{2d^2}{3At_{\max}^2\left(1+\alpha\frac{\Delta j}{j_o}\right)} \tag{1}$$

where μ = mobility ($cm^2/(V\ s)$), d = thickness of the active layer (cm), A = ramp rate of the voltage (V/s), t_{max} = peak extraction time (s), j_0 = capacitive current of the device (a.u.), Δj = height of the CELIV bump as compared to the capacitive current (a.u.), α = correction factor that is experimentally obtained (in our case, α = 0.36). Charge carrier mobility of the non-annealed and the annealed devices calculated using Equation 1 yielded values of about 2.7×10^5 $cm^2/(V\ s)$ and 5.3×10^5 $cm^2/(V\ s)$ respectively. This indicates that the non-annealed devices have bad charge transport resulting in higher recombination and hence these devices have a lower j_{sc} and fill factor. Extracting precise charge carrier mobility values from broad photo-CELIV peaks is difficult. This is attributed to the ambiguity associated with t_{max} in broad peaks [79]. This ambiguity is better understood from the broad bump shown in a study aimed to understand the reproducibility of organic solar cells [80]. In the above mentioned work, a broad photo-CELIV peak is seen to originate from a mismatch of electron and hole mobility. It is known that, mismatch in the electron and hole mobilities is one of the factor which can seriously affect the fill factor of an organic solar cell and in extreme cases (mobility ratio between electron and hole >100) induces an 'S' shape to the j–V curve of the device [81]. As can be seen from Figure 12, the non-annealed sample has a broad photo-CELIV peak suggesting that it has a higher mismatch in electron and hole mobility as compared to the annealed sample. The photo-CELIV transient for the annealed sample has a

very narrow peak and this would mean that the electron and the hole mobilities are quite close to each other. In the non-annealed sample, the bump is much wider suggesting the existence of a higher mismatch between the electron and hole mobilities (in the present study the mismatch is smaller than 100 times as there is no observation of a 'S' shape in the j–V curve). Hence the estimated value for the mobility of the non-annealed sample is an average of its electron and hole mobility. The photo-CELIV transients for both the annealed and non-annealed sample start off similarly but the non-annealed sample is quickly tailed off by a veiled low mobility peak. This clearly suggests that the non-annealed device should have a lower fill factor and it is interesting to note from the j–V curves (Figure 10e) that the non-annealed sample indeed had a lower fill factor of about 42% where as the annealed sample had a fill factor of about 74%. The CELIV peaks are spatially separated and the raise of photo-CELIV transients for both the annealed and the non-annealed samples are similar. This suggests that either the electron or the hole mobility in the non-annealed sample is similar to the average mobility of charge carriers in the annealed sample [80]. Photo-CELIV technique generally cannot identify electron and hole mobilities individually. As the exciton generation and charge separation are similar for both the annealed and non-annealed devices, the EQE data may provide a better picture of the charge transport in these devices. It is evident that the overall EQE is lower for the non-annealed sample as compared to the annealed sample (Figure 11). It is worth pointing out here that the non-annealed sample has a shoulder at around 600 nm in the EQE spectrum and this reveals that the P3HT is crystalline in nature and also the annealed and non-annealed samples show no significant differences in the absorption spectra [58, 82]. This is attributed to the fact that the films were processed using high boiling point solvent o-dichlorobenzene which results in inducing a high degree of ordering within the P3HTdomains causing it to be crystalline in nature [82]. Thermal annealing thus seems to have a pronounced effect on the fullerene phase and much lesser

effect onto the P3HT phase. From the earlier deductions made about the high mismatch in mobilities of electrons and holes in a non-annealed sample sets up the hypothesis that the electron mobility is poor in a non-annealed sample causing the device to perform poorly as compared to an annealed sample. The thermal annealing results in an ordered arrangement of the donor–acceptor phases along with imparting higher crystallinity to the fullerenes in the device which in turn helps to increase the electron mobility. The film morphology gradually reaches an optimised state with balanced charge carrier mobility and this is the reason for the observed higher jsc and high efficiency of 5.9%, measured under simulated AM 1.5 solar conditions. The balanced charge carrier transport also lowers the charge recombination and impedes charge accumulation there by facilitating easy collection of separated charge carriers [83].

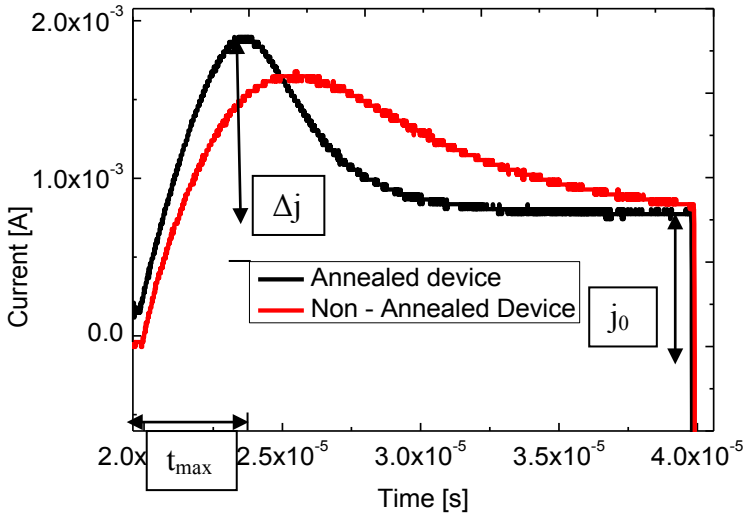

Figure 12 Photo-CELIV transients for non-annealed and annealed (140 °C, 50 min) pseudo bi-layer organic solar cell samples. The charge extracted out of the device upon excitation and extraction is represented in the CELIV bump.

Time of flight-secondary ion mass spectroscopy (TOF-SIMS)

Thus far, the effects of thermal annealing and the inter-diffusion process were investigated through photo-physical studies and electrical characteristics of the pseudo bi-layer device. The findings reported so far suggest that there is an inter-diffusion of ICBA into the P3HT

layer. In order to ascertain this hypothesis, depth profiling of the sample through TOF-SIMS was done on selected samples to study the effect of thermal annealing on the extent of diffusion of ICBA. TOF-SIMS is an analytical technique which is surface sensitive and uses a primary ion beam to desorb, ionise and analyse species from a sample surface [84]. In our experiments we have used a Cs^+ ion gun to remove the top layer and thus enable depth profiling, for the negative TOF-SIMS, the Bi_3^+ analysis gun is fired at the sample and the resultant negatively charged debris were analysed. The charged species were accelerated and identified according to their atomic weight by the mass spectrometer. The results are purely qualitative in nature and not quantitative. Apart from that, the resolution of the depth profiling gets affected when the profiled surface is rough, causing analysis of different depths at the same time and smearing the elemental profiles, never the less, some useful conclusions can still be made from this analysis. It is also important to note that the sputtering time per nanometre depends on the material being analysed and is known to be considerably higher for fullerene than for P3HT and this results in a nonlinear relation between the sputtering time and the depth being profiled as well as different sputter times for different samples with equal thickness. TOF-SIMS was conducted on a set of samples with P3HT as a bottom layer and ICBA as top layer. A solution of ICBA was dropped onto the P3HT layer and then was spin coated after a variable time, 't'. This variable time, 't', is defined as the waiting time period after the ICBA solution was dropped on the P3HT bottom layer and before the spin coating had been started. The three scenario in Figure 13 are as follows: Figure 13a corresponds to t = 0 s (no waiting time) and sample was not annealed after the spin coating, Figure 13b corresponds to t = 30 s (waited for 30 s and later spin coated, sample was not annealed) and Figure 13c corresponds to t = 30 s (waited for 30 s and later spin coated, sample was latter annealed at 140 ºC for 20 min). An isotope of sulphur ($^{34}S^-$) is used as a marker for P3HT [61], C_9^- for ICBA and Si^- was used as a marker for the glass substrate [85]. It can be seen

from Figure 13c, (the sample that was thermally annealed for 140 ºC for 20 min) that the concentration of P3HT and ICBA throughout the thickness of the device remains constant. This suggests that the ICBA has completely inter-diffused and infiltrated the underlying P3HT layer. From the figure it is also clear that the ICBA is almost uniformly distributed within the bulk of the sample and result in similar profiles with no distinct concentration gradient of either material. As can be seen from Figure 13b and c, the P3HT profiles are similar and also, they show a uniform ICBA profile. These observations suggest that the device depicted in Figure 13b does not have any P3HT or ICBA concentration gradient throughout the thickness of the device. Figure 13a and b are not identical in their P3HT profiles. Figure 13a shows a weak increasing P3HT profile which is not similar to the P3HT profiles seen in either Figure 13b or c suggesting that there is a weak interface between the P3HT and ICBA layers in this device whereas Figure 13b has a relatively uniform P3HT profile. Therefore, all the above results show that a waiting time of 30 s before the spin coating of ICBA is enough for the ICBA to diffuse significantly into the P3HT layer.

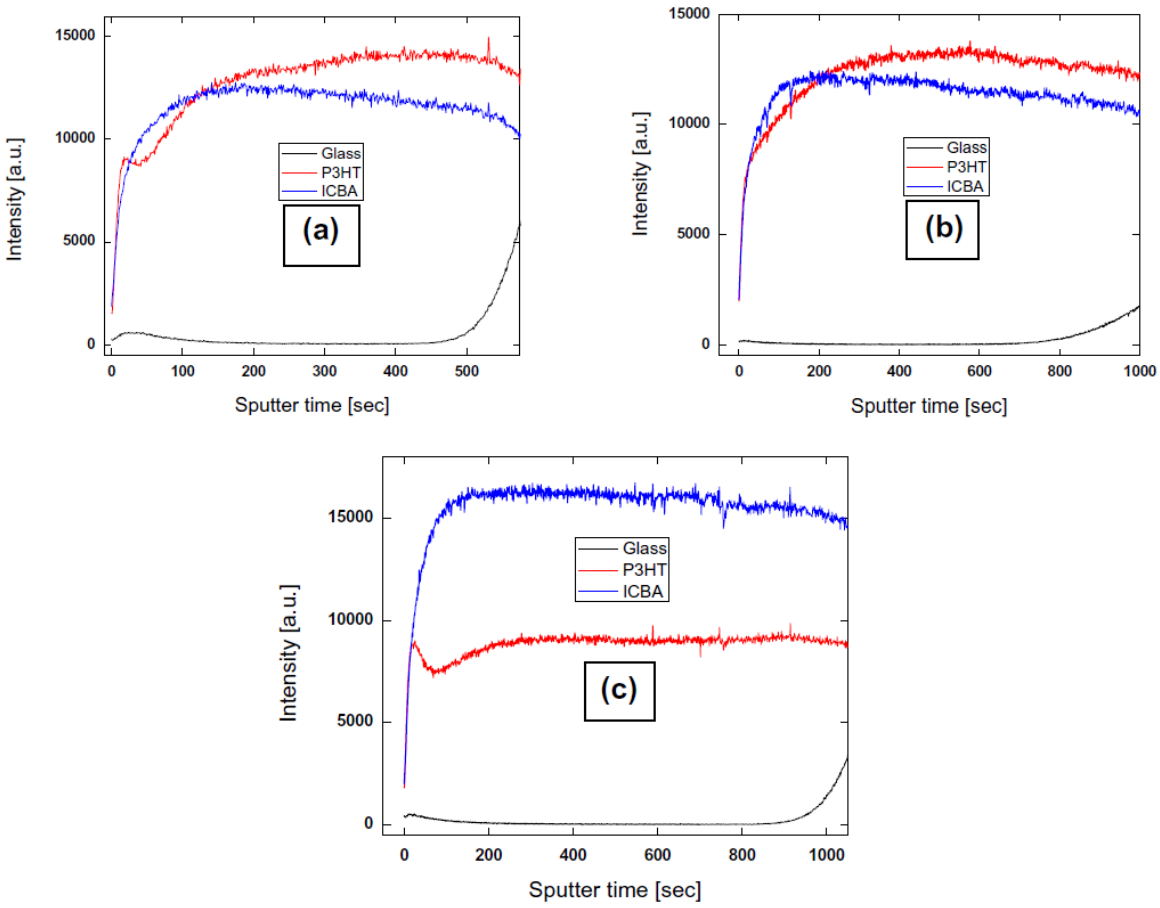

Figure 13 TOF-SIMS was done on samples with a P3HT layer and an ICBA layer on top. A solution of ICBA was dropped onto the P3HT layer and a variable time ''t'' after the solution was dropped, spin coating had been started. (a) t = 0 s (no waiting time) and sample was not annealed, (b) t = 30 s (waited for 30 s) and sample was not annealed, (c) t = 30 s waited and sample was latter annealed at 140oC for 20 min. (a) Weak increasing P3HT profile which is not similar to the P3HT profiles seen in either, (b) or (c) suggesting that there is a weak interface between the P3HT and ICBA layers in the device.

Conclusions

In the work presented above, it was shown that sequentially processed P3HT:ICBA pseudo bi-layer organic solar cells show a certain degree of intermixing even without any heat treatment. Photoluminescence quenching and TOF-SIMS results explicitly confirms that the fullerene inter-diffuse even at room temperature into the P3HT layer. Though, this intermixing leads to efficient exciton dissociation, it does not result in efficient charge carrier extraction. Thermal annealing imparts crystallinity to the fullerene phase and this is reflected in the improvement of charge carrier mobility as ascertained from the photo-CELIV studies and the observation of better short circuit current density and fill factor. The champion

pseudo bi-layer organic solar cell exhibits an efficiency of 5.9% with open circuit voltage of 850 mV, short circuit current density of 9.4 mA/cm^2 and a fill factor of 73.8% under the standard testing conditions of AM 1.5G, 1000 W/m^2. The obtained efficiency is among the highest values reported in the literature for this fabrication route. These pseudo bi-layer organic solar cells have certain advantages over their BHJ counterparts like control over processing conditions, thermal annealing and minimal usage of active components. High performance organic solar cells can be fabricated by this route employing optimum thermal annealing conditions.

Identification of trap-states in OSCs through a modified Photo – CELIV method

As discussed before, the PCE and lifetime of a solar cell is of great importance to make the solar cell economically viable in the current market. In the previous section, a method by which the PCE of OSCs can be increased had been discussed. In this section, a method that would help us identify and evaluate the extent to which a solar cell degrades thereby identifying a solar cell with lesser lifetime (by accelerated degradation tests).

Introduction

Photo – CELIV has been widely used for evaluating charge carrier mobility [86, 87], charge recombination rates [88], charge carrier densities [88], etc. It has been credited as an effective method for evaluating charge carrier mobilities in organic solar cells (OSCs) as this method can be directly performed on an OSC (unlike SCLC or TOF) and this method would give us the charge carrier mobility under charge concentration that are observed in a device under normal operations (1 sun illumination). There has also been some discussion [89, 62] about observing charge trapping from CELIV measurements but there has never been a technique

to identify and evaluate the number of charge traps in an OSC with the help of a CELIV measurement.

Trap-states are critical to the performance of OSCs as they reduce the charge carrier mobility, disturb the internal field distribution and reduce the operational stability of the device [90]. Concerning the lifetime of the devices, the influense of oxygen-related (air related) defect states on the charge transport might be decisive with respect to the long-term stability. The existing and widely used trap identification/estimation methods such as thermally stimulated current (TSC) technique [91, 92] or deep level transient spectroscopy (DLTS) [93] use expensive equipment such as a cryostat to cool the samples to close to zero Kelvin from where they are heated and the current emitted is recorded and associated to trapped charge (in case of TSC). Apart from the cost of the cryostat, it can also be noted that, these techniques take a long time (for sample cooling and progressive heating of the sample) even to identify charge trapping.

The aim of this work is to develop a technique that can quickly and in a cost effective manner, identify and evaluate the number of trap-states in an OSC. The work also aims to validate this technique with a mathematical model. Light bias – CELIV (LB-CELIV), the technique investigated here is used at room temperature and uses a modified Photo-CELIV setup to identify and through fitting the experimental data with a model, estimate the total number of trap states in an aged OSC. This technique hence eliminates the need to use expensive cryostats and is relatively quicker in identifying trap states. The ease of the technique might make it industrially relevant for the quick prognosis of OSCs to weed out defective solar cells after carrying out stability tests.

Sample Preparation

In order to carry out controlled degradation analyses of OSCs, sample A1-A6 are fabricated. A1 being a control sample, was fabricated in the route described previously under the experimental procedures (BHJ sample preparation). Sample A2 through A6, however, were fabricated in a controlled manner that introduces a fixed number of charge traps in the OSCs. This was done by exposing the samples in a clean room to a controlled environment (RH – 45%, 22°C) for a variable amount of time after the active layer was spin coated onto the PEDOT:PSS layer and before the samples were loaded into the evaporator for depositing the cathode layer. This exposes the active layer to ambient oxygen and moisture which induces charge traps in OSCs [94, 95]. This method was preferred over exposing a completed OSC with the metal cathode to ambient atmosphere as then the metal cathode would get oxidized and the degradation effect was not restricted to the active layer only. A description of the samples can be found in Table 2.

Table 2 List of OSC samples and their corresponding exposure to ambient atmosphere to obtain controlled degradation.

Sample Name	Ambient exposure time (minutes)
A1	0
A2	10
A3	20
A4	30
A5	60
A6	120

Experimental setup

The LB – CELIV setup used in this work is schematically shown in Figure 14. The time scales in the LB – CELIV technique is explained in Figure 15. At the beginning of a measurement, the LED is turned on for a time interval, t_1. After a delay time, t_d, a voltage ramp is applied to the sample for a time, t_r. Once the voltage ramp is activated, charges are extracted from the device (similar to in a Photo – CELIV experiment). The respective current is recorded by an oscilloscope (see Figure 14) and the current response is shown by the upper right curve in Figure 15 (drawn in black). The shaded region marked under the bump that appears in the current response represents the charge extracted from the OSC. The internal resistances of both the oscilloscope and the function generator are very small compared to the internal resistance of the solar cell. This will allow the voltage applied by the function generator to be localized across the solar cell (mostly). The solar cell, throughout the experiment, is under short-circuit (applied voltage = 0 V) condition except for when the voltage ramp is applied.

Experimental technique

The experimental technique to identify trap-states is described as follows: A LB – CELIV curve (named LED off) is first taken with the light bias (in this case, an LED) turned off (all along the time, t_1). This part of the technique is similar to a dark – CELIV measurement. Next, the light bias (LED) is turned on for the time, t_1 and a LB-CELIV curve is record (named LED on). In both cases, a time delay (t_d) of 2 ms and a ramp time (t_r) of 10 μs is used. Now, a comparison is made between both the recorded curves and if a "charge extraction" bump is noticed on the "LED on" curve that is bigger than the bump for an "LED Off" curve, it can be concluded that the device has trap-states. The duration of time interval t_1 is not critical, it only needs to be longer than the time necessary for trap saturation whereas the time delay, t_d, is crucial as it needs to be long enough to indicate charge trapping behaviour. From literature [96], it is clear that any time in the millisecond regime is enough to suggest charge

trapping phenomena. Hence, in this experiment, we chose t_1 = 8 ms and t_d = 2 ms (unless mentioned otherwise).

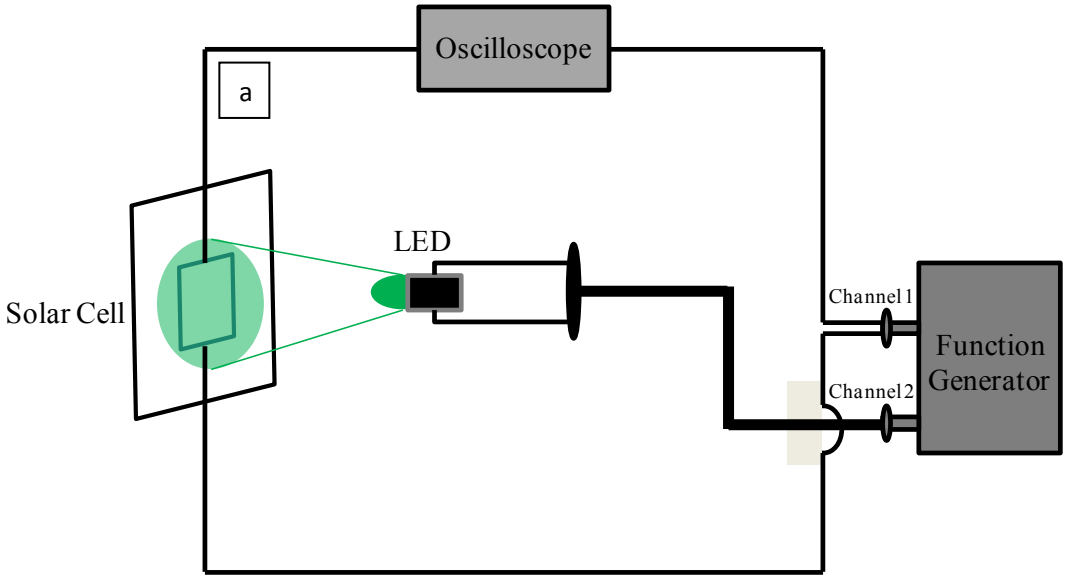

Figure 14 Schematic drawing of the LB – CELIV experimental setup. The LED is activated via channel 2 of the function generator for a time t_1 (see Figure 15). After a time delay of t_d, a voltage ramp is applied across the solar cell (channel 1, duration t_r). The internal resistances of both the oscilloscope and the function generator are small compared with the internal resistance of the solar cell. Therefore, the voltage applied by the function generator is mainly applied across the solar cell. The oscilloscope measures the current response of the solar cell to the voltage ramp applied by the function generator.

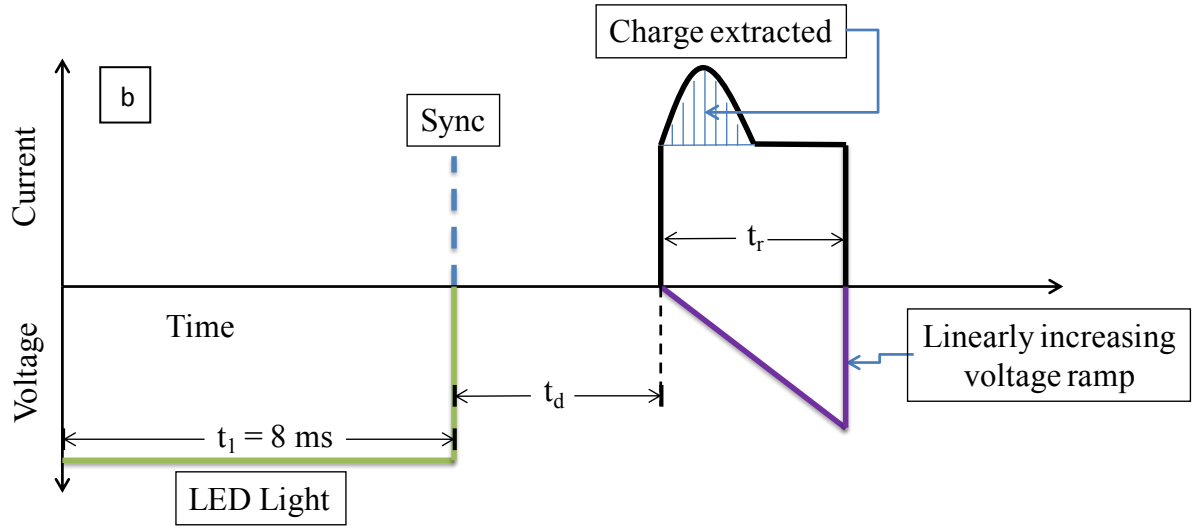

Figure 15 The timing structure of the LB - CELIV technique is schematically explained in this figure. A time of t1 = 8 ms is represented to the left of the figure. This is then followed by a delay time of td = 2 ms and then followed by a linearly increasing voltage ramp for a time or tr = 10 µs. The current response from the solar cell is indicated by the black curve with a shaded region. The shaded region indicates the charge extracted from the device.

Mathematical Model

Before getting into investigating LB-CELIV's experimental results, a mathematical model has been developed using drift diffusion equations in conjuncture with the Poisson's and continuity equations to simulate the LB-CELIV experiment. This way, the model can be fit with the LB-CELIV's experimental results and this would give us device trapping parameters helpful in quantifying the degradation.

The kinetic structure of this model is shown in Figure 16. The model is a modification of other transient models used to analyse OSCs such as transient photocurrent measurements [97, 75], intensity-modulated photocurrent spectroscopy [98] and photo-CELIV [99, 89]. For simplicity, the internal nano structure of the active layer is ignored and instead, the device is modelled by an effective medium approach [100] assuming that the electron (μ_n) and hole

(μ_p) mobilities represent the transport of their respective carriers through PCBM and P3HT components of the blend.

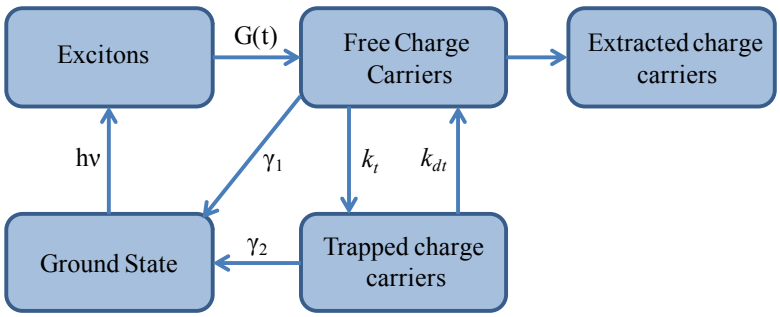

Figure 16 Schematic of the kinetic components of the model used in this work. The schematic includes exciton generation from light (hν), charge generation from excitons ($G(t)$), bimolecular recombination (γ_1), trapping (k_t), trap-assisted recombination (γ_2) and temperature dependant detrapping (k_{dt}) mechanisms.

The model (see Figure 16) assumes that once the solar cell is exposed to light, the light will immediately generate excitons. These excitons then quickly (20 - 1000 ps [101, 102]) diffuse to the P3HT/PCBM interface and dissociate into bound electron-hole (b-e-h) pairs. These b-e-h pairs, then, either dissociate into free charges or decays (germinate recombination) to its ground state [103, 104]. The dissociation into free charge takes around 200 fs [105]. These free charges, are generated at a rate of $G(t)$ (90% of b-e-h pairs dissociate to give free charge carriers under short circuit conditions [100, 44] thereby substantiating our assumption that the charge generation rate is equal to the exciton generation rate). They then get trapped (k_t), undergo bimolecular recombination (γ_1) and/or are extracted from the cell. The trapped charges can further undergo recombination from within the trap-states (also called as trap-assisted recombination (γ_2) [98, 106-108]) or de-trap (k_{dt}) to become free (or mobile) charges again [107]. Charge transport and de-trapping occur in the microsecond to millisecond time regime [96]. Hence, while capturing the trapping and de-trapping phenomena (occurring in micro-millisecond regime) in a transient model, one can ignore the faster processes such as exciton diffusion and b-e-h pair dissociation. Additionally, it is also assumed that trap-states

are electron traps only. This choice simplifies the model and is also in line with the existing literature [97, 98, 106-108]. Below is a list of all the equations used in the model.

Governing Equations

Equation 2 and Equation 3 represent continuity equations for both electrons and holes respectively. These equations have coupled drift-diffusion terms along with a generation ($G(t)$) and a Langevin (γ_1) based bimolecular recombination terms. For electrons, in Equation 2, a trapping term has been included to account for electron loss into traps-states.

Equation 2

$$\frac{\partial n_f(z,t)}{\partial t} = \frac{1}{e}\frac{\partial}{\partial z}\left(\mu_n k_b T \frac{\partial n_f(z,t)}{\partial z} + \mu_n n_f(z,t) e E(z,t)\right) + G(t) - \gamma_1 n_f(z,t) n_p(z,t) - \frac{\partial n_t(z,t)}{\partial t}, \quad (2)$$

Equation 3

$$\frac{\partial n_p(z,t)}{\partial t} = \frac{1}{e}\frac{\partial}{\partial z}\left(\mu_p k_b T \frac{\partial n_p(z,t)}{\partial z} - \mu_p n_p(z,t) e E(z,t)\right) + G(t) - \gamma_1 n_f(z,t) n_p(z,t) - \gamma_2 n_t(z,t) n_p(z,t), \quad (3)$$

The z- direction is assumed to be in the direction from the cathode (negative electrode, $z = 0$) to the anode (positive electrode, $z = L$). The parameters (including their numerical values) used in the mathematical model are summarised in Table 3.

Equation 4 describes the dynamics of charge trapping. A trapping rate constant, k_t, detrapping rate constant, k_{dt} and a trap-assisted recombination rate constant, γ_2, are coupled in this equation to account for the charge trapping, detrapping, recombination and trap-assisted recombination that occurs with free electrons in the presence of N_t trap-states. This process is also depicted in Figure 16.

In Equation 5, the total electron density, *n(z,t)*, is represented as the sum of the trapped electrons, $n_t(z,t)$, and free/mobile electrons, $n_f(z,t)$.

Equation 4

$$\frac{\partial n_t(z,t)}{\partial t} = k_t n_f(z,t)(N_t - n_t(z,t)) - k_{dt} n_t(z,t) - \gamma_2 n_t(z,t) n_p(z,t), \quad (4)$$

Equation 5

$$n_f(z,t) + n_t(z,t) = n(z,t), \quad (5)$$

Equation 6 is a Poisson's equation that describes the electric field profile inside the device due to space charge.

Equation 6

$$\frac{\partial E(z,t)}{\partial z} = \frac{e}{\epsilon_0 \epsilon_r}\big(n_p(z,t) - n(z,t)\big), \quad (6)$$

Constitutive relations

Equation 7 is used to calculate the Langevin bimolecular recombination rate constant. It is assumed that trap-assisted recombination also takes the form of Langevin recombination and hence Equation 8 gives us this recombination rate constant.

Equation 7

$$\gamma_1 = e\left(\frac{\mu_n + \mu_p}{\epsilon_0 \epsilon_r}\right), \quad (7)$$

Equation 8

$$\gamma_2 = k_{\gamma_2} \gamma_1, \quad (8)$$

Equation 9 describes the temperature dependence of the de-trapping rate constant [109].

Equation 9

$$k_{dt} = k'_{dt} e^{\frac{-\Delta E}{k_b T}}, \tag{9}$$

Equation 10 is the Einstein's relation relating the charge diffusion coefficient ($D_{n,h}$) to the respective mobilities.

The charge generation rate as required to simulate LB – CELIV is represented by Equation 11 and Equation 12 indicates the linearly increasing voltage ramp, with a maximum voltage of (V_{max}) that is simulated to extract charges out of the device. It is also important to note here that the device is kept under short-circuit condition for a time period of $t_1 + t_d$. Equation 13 takes into account that the LED is turned off before the charge is extracted from the device and the ramp time used in this experiment is 10 µs.

Equation 10

$$D_{n,h} = \frac{\mu_{n,h} k_b T}{e}, \tag{10}$$

Equation 11

$$G(t) = \begin{cases} G^0, & t < t_1 \\ 0, & t \geq t_1 \end{cases}, \tag{11}$$

Equation 12

$$V_a(t) = \begin{cases} 0, & t < t_1 + t_d \\ \frac{V_{max}}{t_r}(t - t_d), & t \geq t_1 + t_d \end{cases} \tag{12}$$

Equation 13

$$t_r = 10^{-5}\text{s} \tag{13}$$

Finally, the current density (J_{tot}) extracted from the device is evaluated by Equation 14.

Equation 14

$$J_{tot} = \mu_n \left(k_b T \frac{\partial n_f}{\partial z} + n_f e E \right) + \mu_p \left(k_b T \frac{\partial n_p}{\partial z} - n_p e E \right) \quad (14)$$

Table 3 List of parameters, their symbols and their numerical values. In the list below, "Fitted" refers to numerical values of parameters obtained by data fitting (sample A6), "Evaluated" refers to the parameter values obtained by using the constitutive relations (eqn.6 – 9), "Constant" refers to universal constants, "Obtained" refers to values obtained from literature and "Experimental" refers to the experimentally fixed parameters.

Parameters	Symbols	Source	Numerical values
Mobility of electrons	μ_n	Fitted	2.4×10^{-9} $m^2.V^{-1}.s^{-1}$
Mobility of holes	μ_p	Fitted	1.6×10^{-9} $m^2.V^{-1}.s^{-1}$
Boltzmann constant	k_b	Constant	1.38×10^{-23} $m^2.kg.s^{-2}K^{-1}$
Temperature	T	Experimental	296 K
Elementary charge	e	Constant	1.609×10^{-19} A.s
Free charge generation rate	$G°$	Fitted	1×10^{25} $m^{-3}.s^{-1}$
Bimolecular Langevin recombination rate constant	γ_1	Evaluated, eqn. (6)	2.4×10^{-17} $m^3.s^{-1}$
Trap-assisted recombination rate constant	γ_2	Evaluated, eqn. (7)	7.8×10^{-18} $m^3.s^{-1}$
Trapping rate constant	k_t	Fitted	1.6×10^{-16} $m^3.s^{-1}$
Density of trap states	N_t	Fitted	2.2×10^{25} m^{-3}
Detrapping rate constant	k_{dt}	Fitted	1.4×10^{5} s^{-1}
Permittivity of free space	ϵ_0	Constant	8.85×10^{-12} $A^2.s^4.m^{-3}.kg^{-1}$
Relative permittivity	ϵ_r	Obtained [12, 36]	3
Maximum applied voltage	V_{max}	Experimental	4 V

Pre-factor for de-trapping rate constant	k'_{dt}	Evaluated, eqn. (8)	7×10^{6}
Average depth of trap-states	ΔE	Obtained [28]	0.1 eV
Density of states	$N_1=N_{cv}$	Obtained [12, 36]	2.5×10^{25} cm^{-3}
Number of filled charge states	N_2	Obtained [12]	10^{10} cm^{-3}
Effective band gap	E_g	Obtained [12, 19]	0.9 V
Trap assisted recombination rate pre-factor	$k_{\gamma 2}$	Fitted	0.32
Device thickness	L	Experimental	1.3×10^{-7} m
Electron Diffusion coefficient	D_e	Evaluated, eqn. (9)	4.1×10^{-11} $m^2.s^{-1}$
Hole Diffusion coefficient	D_h	Evaluated, eqn. (9)	6.1×10^{-11} $m^2.s^{-1}$

Boundary conditions

It is assumed that there is a perfect alignment between the HOMO of P3HT and the work function of ITO ($z=L$). It is also assumed that the LUMO of PCBM matches perfectly with the work function of the aluminium cathode ($z=0$). This is generally valid for the materials chosen to conduct this study [110, 111]. Equation 15 illustrates that boundary condition. A Neumann boundary condition, on the other hand is assumed in the case of the trapped charges (for Equation 4). This is represented in the form of Equation 16. The voltage boundary condition used for the Poisson's equation, is shown in Equation 17.

Equation 15

$$n_{e,h} = \begin{cases} N_{1,2}, & z = 0 \\ N_{2,1}, & z = L \end{cases} \tag{15}$$

Equation 16

$$\frac{\partial n_{et}}{\partial x} = 0 \; for \; z = 0, L \tag{16}$$

Equation 17

$$\square = \begin{cases} 0, & z = 0 \\ V_a - E_g, & z = L \end{cases} \tag{17}$$

A brief description of the different time regimes in the LB – CELIV experiment is shown in Table 4. Here, the various states of charge generation, applied voltage and the extracted current are mentioned along with the respective time that they are active for is indicated.

Table 4 Summary of the various regimes of the LB - CELIV's operation under light bias (LED-on) and during the dark (LED-off) at various times throughout the LB – CELIV's process. *G*°, represents the free charge carrier generation rate when the LED is turned on. *VR*, indicates the voltage ramp applied to extract charges from the cell. SC means short-circuit termination of the cell and *CE*, represents the current extraction mode under quasi short circuit conditions.

	Time (t_1)	Time (t_d)	Time (t_r)
Generation of free charge carriers LED-on / LED-off	*G*° / 0	0 / 0	0 / 0
Applied voltage LED-on / LED-off	0 / 0	0 / 0	*VR*/*VR*
Current Extraction LED-on / LED-off	*SC*/*SC*	*SC*/*SC*	*CE*/*CE*

Numerical methods

COMSOL multiphysics 3.5a, a commercial finite-element software was employed to solve the set of differential equations shown above. The data from experiments was fitted to the model prediction by applying a pattern search algorithm to obtain free parameters ($G°$, N_t, k_t,

k_{dt}, $k_{\gamma 2}$, μ_e and μ_p). During the fitting, care was taken to make sure that the parameters obtained were able to predict results for two t_1 values and for two t_d values (for a given t_1). The model was validated by comparing experimental results (other than the ones used for fitting procedures) with model predictions done by parameters that were obtained through fitting procedures. This is further illustrated and discussed in the results and discussion section.

Results and Discussion

Current density - voltage characteristics (J-V)

Devices A1 through A6 were fabricated using the procedure described before and were tested under one sun conditions. The efficiency results are shown in Figure 17 and the corresponding J-V data is given in Table 5. From this data, it is evident that exposure of the sample to ambient conditions (before contact formation and encapsulation) degrades the solar cells. The parameter that is affected the most is the fill factor (FF). The effect that such an exposure has on the performance of OSCs has been previously reported [98, 106, 112].

Table 5 List of various J-V parameters for solar cells with increasing ambient exposure starting from A1 to A6 are shown here. An explanation of the various sample treatments is given in Table 2. A total of at least 10 solar cells were used to obtain the statistical information presented in the table below.

	A1	A2	A3	A4	A5	A6
V_{oc} (V)	0.61 ± 0.01	0.59 ± 0.01	0.59 ± 0.01	0.59 ± 0.01	0.56 ± 0.05	0.54 ± 0.01
J_{sc} (mA/cm^2)	5.4 ± 0.7	6.1 ± 0.4	5.9 ± 0.4	4.6 ± 0.8	5.0 ± 0.8	5.3 ± 0.4
FF (%)	59 ± 2	58 ±1	57 ± 1	44 ± 6	46 ± 9	49 ± 1
Eff. (%)	1.9 ± 0.3	2.1 ± 0.2	2.0 ± 0.2	1.2 ± 0.3	1.3 ± 0.4	1.4 ± 0.1

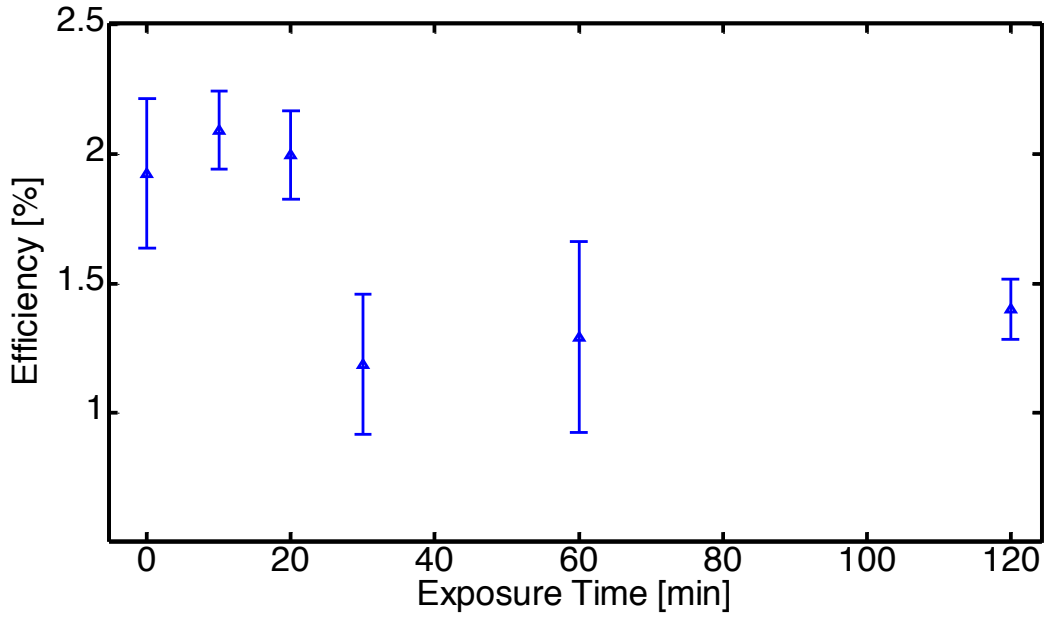

Figure 17 Plot of device efficiency values against exposure (to ambient atmosphere that includes oxygen and moisture) time shows that an increased exposure time leads to a degraded solar cell performance. The data presented here was averaged over at least 10 solar cells.

Trapped charge identification

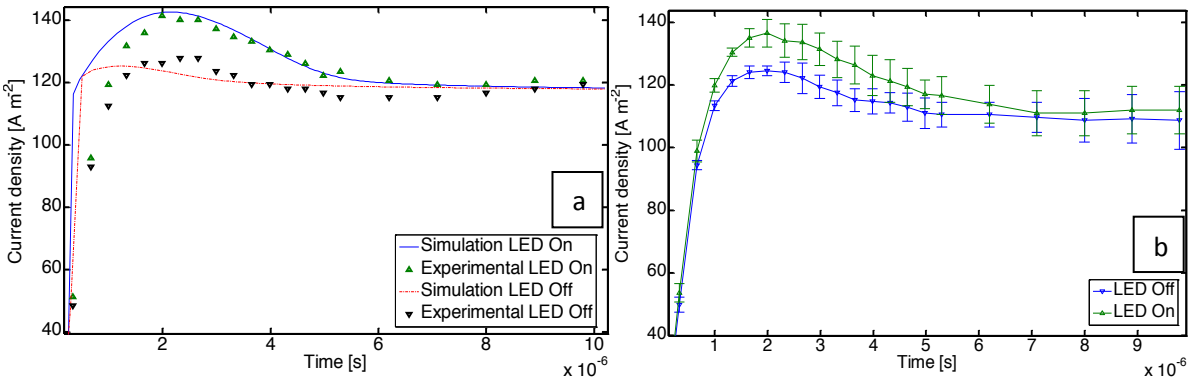

Figure 18 Identification of trapped charges by LB – CELIV (a) Shows a comparison of simulation and experimental results for sample A5 both for LED-ON and LED-Off. (b) A typical experimental result indicating the statistical significance of the LB – CELIV measurements (one standard deviation of 3 measurements is shown). The time axis starts after $t_1 + t_d$ and extends for a time interval of t_r. This applies to Figure 18a and b.

In order to confirm the reproducibility of the experiment, LB – CELIV experiments were first conducted on three devices of the type A5 (see Table 2). The results of these experiments are shown in Figure 18b. It is evident from this figure that, consistently, degraded OSCs of the

type A5 show a bigger bump when they are exposed to light even after the light is turned off for 2ms prior to when the voltage ramp is applied. This statistical finding eliminates the possibility that we are studying an outlier.

The model described above is calibrated to A5 and is used to qualitatively validate the trapped charge identification experimental technique described previously in the instrumentation section. The model predictions presented in Figure 18a concur with the experimental findings qualitatively validating the model.

Extracting parameters through fitting

The above described model is calibrated with the help of experimental data from samples A1 through A6. It is important to note here that the model was first calibrated with LB – CELIV transients obtained from each sample at different delay times. Upon calibration, model parameters such as electron and hole mobilities, total number of trap-states, trap-assisted recombination rate constants, trapping rate constant and de-trapping rate constant were obtained. Once the parameters were obtained, they were then used to predict the transients for when the LED light was turned on with a delay time of 2 ms. Figure 19a shows experimental data fitted with the model predictions for samples A1, A4, A5 and A6. It is evident from this figure that the model predictions are very close to the experimental findings. The discrepancy between model predictions and the experimental data that exists at the beginning of the CELIV transient is mainly due to the lack of a series resistance parameter in the model that takes into account the series resistance of the circuit coming from connecting wires, oscilloscope's internal resistance, contact resistance, etc. It has been theoretically shown before that the slope of the CELIV curve at the beginning heavily depends on the series resistance of the circuit [99]. At lower series resistance (0 ohms), the slope is close to infinity (implying an almost vertical line) and as the resistance increases, the slope reduces.

Though the bump seen for sample A1 in the LB – CELIV transient, is very small, the model fitting has revealed it to have a significant amount of trap-sates, though much lesser than when compared to A6. This finding is supported by literature presented elsewhere [89, 76, 113]. Among all the parameters that were fitted, the total number of trap-states is plotted against the degradation time in Figure 19b and from this figure, it can be seen that an increased exposure time corresponds to an increased number of trap-states. This numerical data quantitatively validates the findings from the LB – CELIV method. Furthermore, this section also elucidates the capability of this model along with the experimental technique in determining the total number of trap-states in a device.

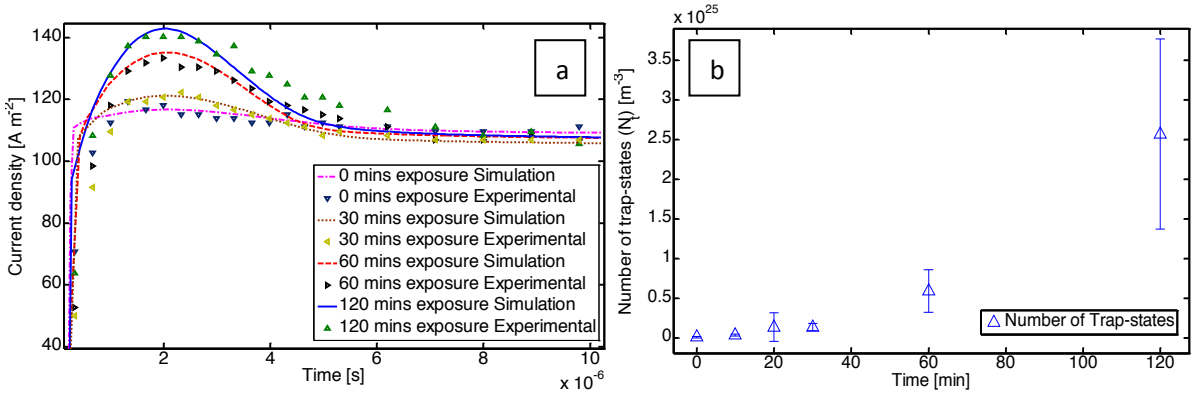

Figure 19 a) Simulated and experimental results (for t_d = 2 ms) obtained from devices A1 (0 mins exposure), A4 (30 mins exposure), A5 (60 mins exposure) and A6 (120 mins exposure). As the degradation time increases, the CELIV bump height, also progressively increases b) Deduced total number of trap-states as a function of the degradation time. The values shown here indicate an average of at least 5 solar cells.

Simulation results

This section gives simulation results obtained from a calibrated model for sample A5. Figure 20a (including Figure 18a and b) indicates a bump in the LB – CELIV transient carried out when the LED is turned off (this is similar to a dark-CELIV measurement). This is not strange to find as it has been previously reported both experimentally [62] and theoretically [89] that devices exhibiting charge trapping behaviour often show a bump under dark conditions. Hence the simulation of the LED-Off CELIV transient (dark-CELIV) showing a bump is a further validation to the model presented in here.

Figure 20b, depicts the trapped charge concentration (n_{et}) against the duration of the LB-CELIV experiment (10 ms) carried out (with LED on) on sample A5. This figure clearly indicates that the total number of trapped charge in the device increases for the first 8 ms for which the device is being exposed to light. Then, after the LED is turned off, since the device is under short-circuit condition, trapped charge is lost by de-trapping, trap assisted recombination and charge extraction from the device till a voltage ramp is applied to the device to further remove trapped charge at a higher rate. This result also indicates that the "charge extraction" bump associated with the LB – CELIV transient measured under LED on conditions is associated with trapped charge.

Figure 20c, indicates theoretical LB-CELIV responses (LED on) carried out on two samples that possess different trap-state concentrations (physically, it translates to a different extent of degradation with the lesser trap concentration representing a sample exposed to ambient atmosphere for a shorter duration of time). This plot clearly indicates that the bump height is indicative of the number of charge traps present in a device.

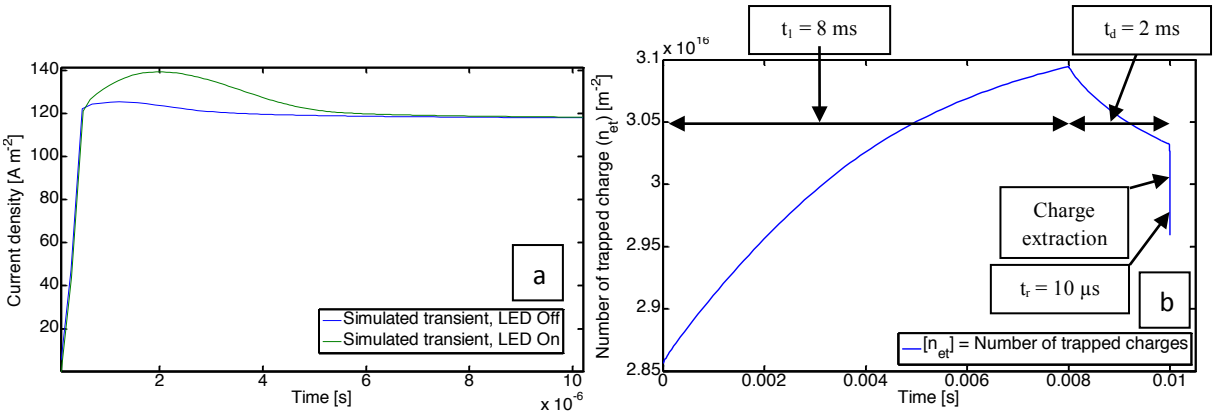

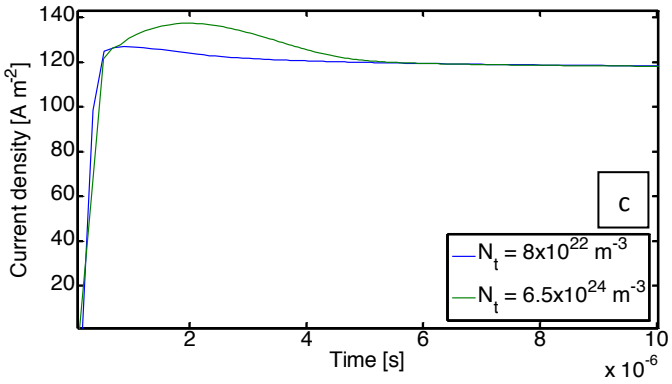

Figure 20 (a) Simulated LB – CELIV results performed with parameters from sample A5 for when the LED is turned on and turned off (b) Shows the evolution of the simulated trapped electron concentration. The time axis starts at t = 0 and extends for a time interval of t1 + td + tr (c) Indicates the difference between the simulated LB – CELIV results for two cases where the total trap-state concentration is different.

Varied time delay effect on LB – CELIV transients

In this section, the time scales of charges that are being extracted from sample A5 while performing the LB – CELIV experiment are investigated. The time delay (t_d) used in LB – CELIV is therefore varied as it gives an indication to the charge carrier life time in the device (Figure 21b). It is also important to note that the time scales for mobile charges in OSCs are around 20 µs - 50 µs [114-115].

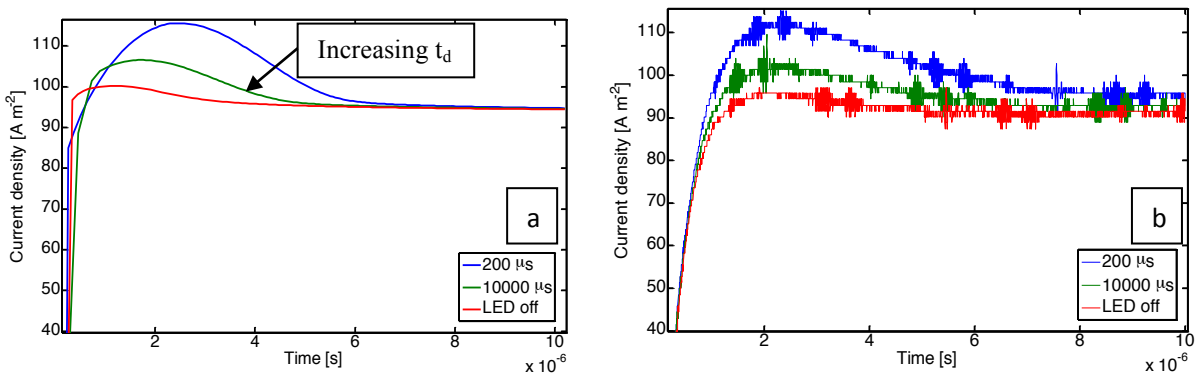

Figure 21 (a) Simulated LB-CELIV responses at two different time delays (t_d) for a device of type A5; (b) Current transients obtained from LB – CELIV experiments for two delay times (sample A5) along with dark CELIV transient.

While carrying out LB – CELIV on sample A5, the sample is exposed to LED light for t_1 = 80ms. A higher time t_1 is used in this experiment to indicate that this experiment can identify trapped charge independent of time t_1. During this time, mobile and trap electronic states are

filled up in the device and then the light is turned off. Since the device is kept under short-circuit condition after the LED is turned off, all the mobile charges are continuously being removed from the sample. Those charges that are inside trap-states, on the other hand, recombine, de-trap or remain trapped. This means that as the delay time increases, charges with higher life time will start de-trapping and become mobile (due to continuous de-trapping) and if a voltage ramp is applied at this stage, these freshly de-trapped charges along with the high life time trapped charges would be removed from the device. Since de-trapped mobile charges can undergo non-germinate recombination (bimolecular recombination) or get extracted due to short-circuit condition present before the voltage ramp is applied, the removed charges through the voltage ramp indicate a lower bound of the total number of trap-states in the device at the time when the voltage ramp is applied. From Figure 21b, it is evident that charges inside the device stays for at least 10ms after the LED is turned off and based on work presented elsewhere [96], charges associated with sub-microsecond to millisecond life times corresponds to trapped charges.

In order to qualitatively validate the numerical model previously presented, a simulation is made keeping all parameters constant and varying the delay time only. The data is presented in Figure 21a. The model has already been calibrated to A5 and hence gives us qualitative information regarding the LB – CELIV transients for this sample. It is evident from Figure 21a that increasing the delay times causes the LB – CELIV peak (bump) to reduce significantly in intensity. Hence, the model is qualitatively validated as its predictions are similar to the experimental findings. Now, if the total number of trap-states are reduced (to the order of 10^{23} m^{-3}), the bump intensities do not change much (not shown here) with varying delay times. This finding points to LB – CELIV being an apt method to study the life time of trapped charges in degraded samples as well.

Temperature dependence of trapped charge extraction

In order to further correlate the charges observed in an LB – CELIV experiment to trapped charges, an experiment was conducted on sample A6 at the following temperatures: 8°C and 32°C. In order to control the temperature of sample, it was placed on an electrically controlled peltier cooler inside the LB – CELIV setup.

The results of the experiment are shown in Figure 22b. Unfortunately, the statistical significance of the data is not very high. This is mainly due to the low temperature range that the peltier cooler works within. The experimental results, on a different note, give a clear indication that the de-trapping rate and thus the extracted charge is temperature dependent (Equation 9).

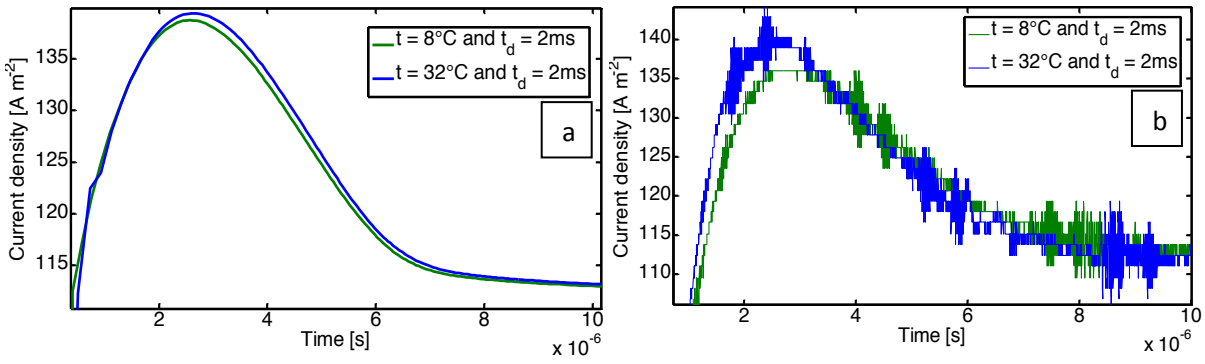

Figure 22 a) Model predictions of LB – CELIV transients for a sample with traps at 8°C (lower curve, green) and 32°C (blue); b) Experimental LB - CELIV transients for sample A6 at ~8°C (lower curve, green) and ~32°C (blue).

From the explanation for thermally stimulated current [116], it is known that heating a sample with trapped charges causes the trapped charges to de-trap (as thermal energy is gained by charges upon heating). When samples are heated, their rate of de-trapping increases and the same thing happens when the voltage ramp is applied also. Hence, one would expect the LB – CELIV bump to be higher for when the temperature is high as opposed to when the temperature is lower. This result is also depicted in the simulation result (Figure 22a).

Conclusions

A new technique, light biased-CELIV (LB – CELIV), is presented here that can easily quantitatively determine the trap concentration in OSC devices with the use of a relatively simple experimental setup. It is similar to that used in Photo – CELIV (photo-induced carrier extraction by linearly increasing voltage) experiments; the main difference is the application of a ms-pulsed LED instead of a short laser pulse. In order to analyse the experimental data a drift-diffusion model that includes trap dynamics and trap assisted recombination was developed. The technique was validated by various experiments such as varied time-delay and varied temperature experiments.

For a set of non-degraded and increasingly degraded bulk hetero-junction OSCs the trap density and other relevant parameters (like trapping and de-trapping parameters) could be extracted from the experimental data. Trap concentrations between 10^{23} m^{-3} and 10^{25} m^{-3} have been found.

Chapter 5

Conclusions

Firstly, it was established that pseudo bilayer architecture was suitable in obtaining high efficiency OSCs due to a better nano-morphology that is made possible in the solar cell through this new fabrication process. Secondly, it was established that, in the case of ICBA based pseudo bilayer solar cells (unlike PCBM), the ICBA diffuses into the underlying P3HT layer without any heat treatment and hence the reason for improved efficiency could not solely be intermixing of the donor and acceptor materials. Further investigations such as EQE, PL, TOF-SIMS and Photo-CELIV have suggested that the reason ICBA based pseudo bilayer solar cells take longer annealing time to achieve optimal efficiency is due to the larger amount of energy that ICBA (over PCBM) takes to crystallize in the pseudo bilayer structure. This was an unexpected result considering that both the acceptor material have fullerene as their backbone.

Moving on from high efficiency, in this thesis, a new technique (LB-CELIV) has been introduced to investigate the extent of degradation occurring in OSCs. This technique could be vital in weeding out underperforming solar cells in an industrial setup.

In this part of the thesis, LB-CELIV was introduced and explained. Experiments such as varied time delay, identifying trap-states, etc. were used as supporting findings to suggest that the charge extracted through LB-CELIV is in fact trapped charge. Apart from this, a 1-D mathematical model with trap-states and trap-assisted recombination was introduced to support the experimental findings. Other than that, the model was also used to fit the experimental data. This gave rise to parameters such as electron and hole mobilities, trapping rate constant, de-trapping rate constant, trap-assisted recombination pre-factor and total number of trap-states. This fitting has not only given us the ability to validate our experimental findings but also has allowed us to quantify the extent of degradation.

Future works

Focused donor material degradation studies

As future work to follow the work presented in this thesis, I would like to propose the use of the pseudo bilayer fabrication process to conduct a focused study on the P3HT or donor material's air stability. This can be done by fabricating the pseudo bilayer as described in the experimental section but before depositing the PCBM or ICBA layer on top of the P3HT layer, the sample would be brought outside the glovebox to undergo controlled degradation. This would allow us to perform targeted degradation on the P3HT layer alone without disturbing the acceptor layer. Once this is done, LB-CELIV could be employed to evaluate the number of trap-states in the solar cell. A better model that includes trap-states in the donor material can be built to fit with the experimental data. This would allow us to more fairly study the donor material's susceptibility to degradation caused by the air.

Apart from that, another variation would be to replace PEDOT:PSS, which has previously been reported to absorb moisture, with an inorganic layer such as MoO_x [117]. This would further focus the degradation in the P3HT layer.

Fabrication of air-stable solar cells without encapsulation

Another experiment that I propose to carry out is the replacement of the anode and cathode buffer layer (in this case PEDOT:PSS and LiF respectively) with low temperature solution processed layers such as MoO_x [118] and TiO_x [119] respectively. A cross sectional image of the solar cell is shown in Figure 23a. For this stack to work as a solar cell, each layer's energy band must cascade such that both electrons and holes can be transported out of the solar cell. The energy band diagram shown in Figure 23b suggests that the material combination used is energetically favourable for charge transport.

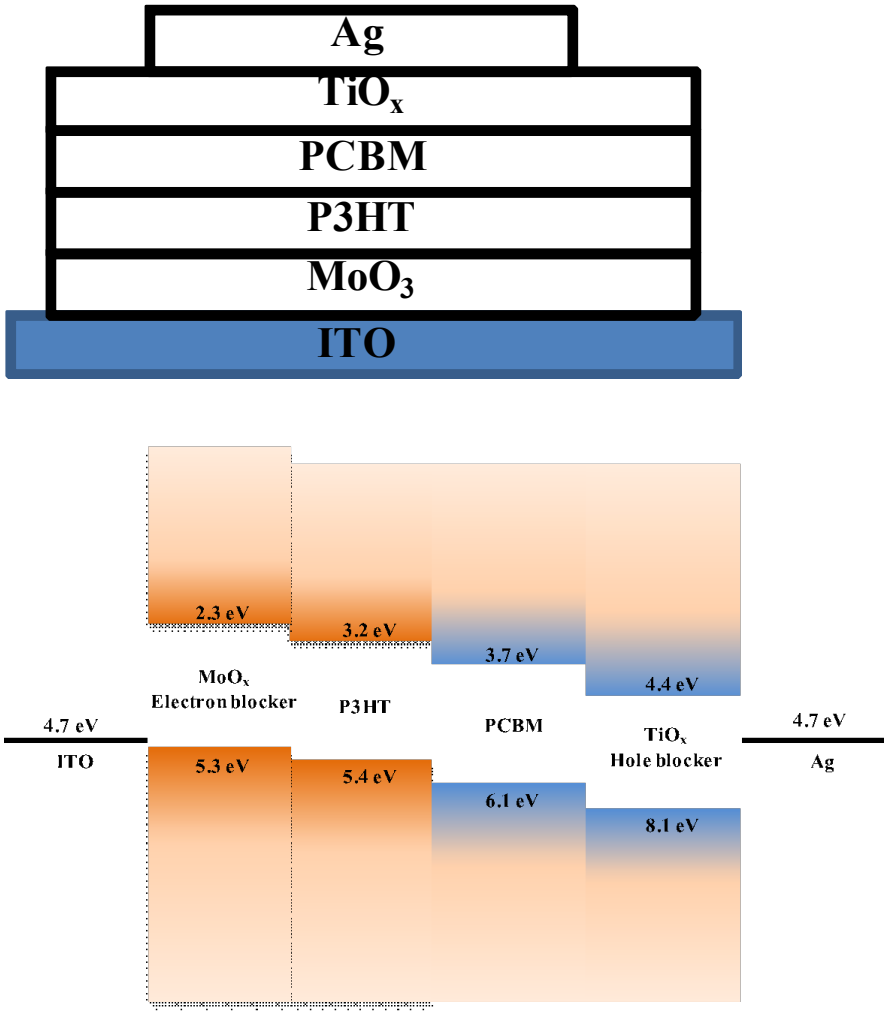

Figure 23 (a) Indicates a cross-sectional view of the proposed solar cell's stack. (b) Indicates the energy band diagram of the solar cell shown in part (a) of this figure. This shows how the energy bands are cascading down forming a potential working solar cell.

The advantage of this structure is that it would not only make the solar cell closer to being fully solution processed but the TiO_x layer on top of the PCBM layer can also act as a protective layer preventing the organic layer underneath from getting damaged from atmosphere oxygen and moisture. It has previously been seen that a layer of PEDOT:PSS coated on top of an inverted OSC had tremendously increased its stability in air [119]. Apart from that advantage, a bilayer method of fabricating the active layer would increase the solar cell's efficiency also.

Once this is done, a comparison can be made between an OSC fabricated in the method mentioned above, OSC that is sealed using an epoxy encapsulation and an un-encapsulated

device. The comparison would be based on their LB-CELIV responses. The total number of trap-states evaluated for each device through model fitting would give us an idea of the effectiveness of each of the sealing process (as compared to the un-sealed device).

Bibliography

[1] http://www.sandia.gov/~jytsao/Solar%20FAQs.pdf (As seen on 02/04/2014)

[2] http://www.solareworld.com/2011/08/09/solar-history-bell-labs-and-the-first-modern-silicon-solar-cell/ (As seen on 02/04/2014)

[3] http://elibrary.worldbank.org/doi/pdf/10.1596/1813-9450-5845 (As seen on 02/04/2014)

[4] http://www.pv-tech.org/news/more_than_1gw_new_solar_installed_by_india_in_2013 (As seen on 02/04/2014)

[5] http://www.ema.gov.sg/page/32/id:65/ (As seen on 02/04/2014)

[6] http://www.ema.gov.sg/media/files/facts_and_figures/2012.03/MSC1.pdf (As seen on 02/04/2014)

[7] http://www.abc.net.au/news/2011-09-07/solar-industry-celebrates-grid-parity/2875592/?site=sydney (As seen on 02/04/2014)

[8] http://www.pv-magazine.com/news/details/beitrag/multicrystalline-silicon-modules-to-dominate-pv-industry-in-2014_100013222/#axzz2xnqCyAFo (As seen on 03/04/2014)

[9] http://cleantechnica.com/2013/10/29/multicrystalline-silicon-modules-dominate-solar-pv-industry-2014/ (As seen on 03/04/2014)

[10] Chittick R, Sterling H, in Adler D, Fritzsche H, Eds, Plenum Press, New York, NY, 1–11 (1985).

[11] Spear W, LeComber P, Solid State Commun. 17, 1193 (1975).

[12] Carlson D, Wronski C, Appl. Phys. Lett., 28, 671 (1976).

[13] Fritzsche H, Mater. Res. Soc. Symp. Proc. 609, A17.1.1–12 (2001).

[14] Schiff E, J. Non-Cryst. Solids, 190, 1 (1995).

[15] Bill Nemeth, Yueqin Xu, Haorong Wang, Ted Sun, Benjamin G. Lee, Anna Duda and Qi Wang, work presented at Materials Research Society Spring Meeting San Francisco, California, April 25-29 (2011).

[16] M. Stuckelberger, M. Despeisse, G. Bugnon, J. W. Schuttauf, F. J. Haug, and C. Ballif, Journal of Appl. Phys., 114, 154509 (2013).

[17] K. Tennakone, G.R.R. Kumara, I.R.M. Kottegoda, V.S.P. Perera, Chem. Commun. 15 (1999).

[18] K. Sayama, H. Suguhara, H. Arakawa, Chem. Mater. 10 (1998) 3825.

[19] Burschka, J.; Dualeh, A.; Kessler, F.; Baranoff, E.; Cevey-Ha, N.- L.; Yi, C.; Nazeeruddin, M. K.; Grätzel, M., J. Am. Chem. Soc. 2011, 133, 18042−18045.

[20] Joseph Kalowekamo, Erin Baker, Solar Energy, 83, Pages 1224‑1231 (2009).

[21] Jihuai Wu, Zhang Lan, Sanchun Hao, Pingjiang Li, Jianming Lin, Miaoliang Huang, Leqing Fang, and Yunfang Huang, Pure Appl. Chem., 80, pp. 2241–2258 (2008).

[22] In Chung, Byunghong Lee, Jiaqing He, Robert P. H. Chang and Mercouri G. Kanatzidis, Nature, 485, pp. 486 (2012).

[23] Mukund Ghavre, Owen Byrne, Lena Altes, Praveen K. Surolia, Marcel Spulak, Brid Quilty, K. Ravindranathan Thampi and Nicholas Gathergood, Green Chem., 16, 2252–2265 (2014).

[24] Kim, H.-S.; Lee, C.-R.; Im, J.-H.; Lee, K.-B.; Moehl, T.; Marchioro, A.; Moon, S.-J.; Humphry-Baker, R.; Yum, J.-H.; Moser, J. E, Sci. Rep. 2012, 2, 591.

[25] Lee, M. M.; Teuscher, J.; Miyasaka, T.; Murakami, T. N.; Snaith, H. J. , Science 2012, 338, 643−647.

[26] Julian Burschka, Norman Pellet, Soo-Jin Moon, Robin Humphry-Baker, Peng Gao, Mohammad K. Nazeeruddin & Michael Gratzel, NATURE, VOL 499, 2013, 316-320.

[27] Nam-Gyu Park, J. Phys. Chem. Lett. 2013, 4, 2423−2429.

[28] Henry J. Snaith, J. Phys. Chem. Lett. 2013, 4, 3623-3630.

[29] Editorial, Sol. Energy Mater. Sol. Cells 2008, 92, 371−373.

[30] Lee, M. M., Teuscher, J., Miyasaka, T., Murakami, T. N., Snaith, H. J., Science, 2012, 338, 643−647.

[31] M. A. Green, Crystalline Silicon Solar Cells, Chapter 4.

[32] Photon International, **176** (March 2009).

[33] Tatsuo Saga, NPG Asia Materials **2,** 96–102 (2010).

[34]http://panasonic.co.jp/corp/news/official.data/data.dir/2014/04/en140410-4/en140410-4.html (As seen on 14/04/2014).

[35] M. Kaltenbrunner, M. S. White, E. D. Głowacki, T. Sekitani, T. Someya, N. S. Sariciftci and S. Bauer, Nature Communications **3**, Article number: 770 (2012).

[36] J. Szlufcik, S. Sivoththaman, J. F. Nijs, R. P. Mertens and R. V. Overstraeten, Proceedings of the IEEE, vol. 85, no. 5 (may 1997).

[37] Zhicai He, Chengmei Zhong, Shijian Su, Miao Xu, Hongbin Wu & Yong Cao, Nature Photonics, 6, 591–595 (2012).

[38]http://www.heliatek.com/newscenter/latest_news/neuer-weltrekord-fur-organische-solarzellen-heliatek-behauptet-sich-mit-12-zelleffizienz-als-technologiefuhrer/?lang=en (As seen on 23/04/2014).

[39] Y. Liang, D. Feng, Y. Wu, S. Tsai, G. Li, C. Ray and L. Yu, J. Am. Chem. Soc., **131**, 7792–7799 (2009).

[40] M. C. Scharber, D. Mühlbacher, M. Koppe, P. Denk, C. Waldauf, A. J. Heeger and C. J. Brabec, Adv. Mater., **18**, 789–794 (2006).

[41] S. Gunes, H. Neugebauer and N. S. Sariciftci, Chem. Rev., **107**, 1324−1338 (2007).

[42] G. Zhao , Y. He and Y. Li, Adv. Mater., **22**, 4355–4358 (2010).

[43] Opitz A, Bronner M and Bruetting W 2007 Ambipolar charge carrier transport in mixed organic layers of phthalocyanine and fullerene J. Appl. Phys. 101 063709.

[44] V. D. Mihailetchi, H. X. Xie, B. D. Boer, L. J. A. Koster and P. W. M. Blom, Adv. Funct. Mater. 16 (2006) 699–708.

[45] B. Domercq, J. S. Yu, B. R. Kaafarani, T. Kondo, S. Yoo, J. N. Haddock, S. Barlow, S. R. Marder and B. Kippelen, Mol. Cryst. Liq. Cryst. 481 (2008) 80–93.

[46] B. P. Rand, J. Xue, S. Uchida and S. R. Forrest, J. Appl. Phys. 98 (2005) 124902.

[47] S. E. Shaheen, C. J. Brabec, N. S. Sariciftci, F. Padinger, T. Fromherz and J. C. Hummelen, 78 (2001), 841–843.

[48] G. Li, V. Shrotriya, Y. Yao and Y. Yang, J.App.Phys. 98, 043704 (2005).

[49] V. D. Mihailetchi, L. J. A. Koster, P. W. M. Blom, C. Melzer and B. D. Boer, Adv. Funct. Mater. 15 (2005), 795–801.

[50] J. Zhou, X. Wan, Y. Liu, Y. Zuo, Z. Li, G. He, G. Long, W. Ni, C. Li, X. Su and Y. Chen, J. Am. Chem. Soc., 134 (2012), 16345−16351.

[51] Lin, Y. Z.; Li, Y. F.; Zhan, X. W. Chem. Soc. Rev. 2012, 41, 4245−4272.

[52] S. Makhseed, J. Samuel, Dyes and Pigments 82(2009)1–5.

[53] S. H. Jung, J.H.Choi, S. M. Yang, W. J. Cho, C. S. Ha, Materials Science and Engineering B Solid-State Materials for Advanced Technology 85(2001)160–164.

[54] M. Juricek, P. H.J. Kouwer, J. Rehak, J. Sly, A. E. Rowan, Journal of Organic Chemistry 74 (2009) 21–25.

[55] M. K. R. Fischer, I. Lopez-Duarte, M. M. Wienk, M. V. Martinez-Diaz, R.A.J. Janssen, P.Bauerle, T.Torres, Journal of the American Chemical Society 131 (2009) 8669–8676.

[56] H. Li, F. R. Fronczek, M. G. H. Vicente, Tetrahedron Letters 49 (2008) 4828–4830.

[57] A. L. Ayzner, C. J. Tassone, S. H. Tolbert and B. J. Schwartz, J. Phys. Chem. C**,** 113 (2009)*,* 20050–20060.

[58] M. D. Heinemann, K. Ananthanarayanan, L. N. S. A. Thummalakunta, C. H. Yong and J. Luther, Green, Vol. 1 (2011), pp. 291–298.

[59] M. Jørgensen, K. Norrman, F. C. Krebs, Sol. Eng. Mat. & Solar Cells 92 (2008) 686–714.

[60] R.D. Scurlock, B. Wang, P.R. Ogilby, J.R. Sheats, R.L. Clough, J. Am. Chem. Soc. 117 (1995) 10194.

[61] K. Norrman, M. V. Madsen, S. A. Gevorgyan, and F. C. Krebs, J. Am. Chem. Soc., 132 (2010), 16883.

[62] J. Schafferhans, A. Baumann, A. Wagenpfahl, C. Deibel and V. Dyakonov, Organic Electronics, 11 (2010), 1693.

[63] http://www.seris.sg/Seris/OurServices/Characterisation_Services.html (As seen on 06/08/2014).

[64] J. Nelson, Mater.Today. 14 (2011), 462.

[65] G. Zhao, T. He and Y. Li, Adv.Mater. 22 (2010), 4355.

[66] F. Padinger, R.S. Rittberger, N.S. Sariciftci, Adv. Func. Mat. 13, 85 (2003).

[67] T. Erb, U. Zhokhavets, G. Gobsch, S. Raleva, B. Stühn, P. Schilinsky, C. Waldauf and C.J. Brabec, Adv. Func. Mat. 15, 1193 (2005).

[68] F. C. Jamieson, E. B. Domingo, T. M. Ward, M. Heeney, N. Stingelin and J. R. Durrant, Chem. Sci, 2012, Advance Article DOI: 10.1039/C1SC00674F.

[69] Y. D. Park, S.G. Lee, H.S. Lee, D. Kwak, D.H. Lee and K. Cho, J.Mater.Chem. 21, 2338 (2011).

[70] D. H.Wang, D. G. C., O. Park and J. H. Park and J. Mater. Chem 20, 4910 (2010).

[71] W. Chen, T. Xu, F. He, W. Wang, C. Wang, J. Strzalka, Y. Liu, J. Wen, D. J. Miller, J. Chen, K. Hong, L. Yu and S. B. Darling, Nano.Lett. 11, 3707 (2011).

[72] C. Deibel and D. Vladimir, Rep. Prog. Phys, 73, 096401 (2010).

[73] D. E. Markov, E. Amsterdam, P. W. M. Blom, A. B. Sieval and J. C. Hummelen, J. Phys. Chem. A 109 (2005),5266.

[74] J.M. Nunzi, C.R Phys 3 (2002), 523.

[75] R. C. I. MacKenzie, C. G. Shuttle, M. L. Chabinyc, J. Nelson, Adv. Energy Mater., 2 (2012), 662.

[76] R.C.I. MacKenzie, T. Kirchartz, G.F.A. Dibb, J. Nelson, J. Phys. Chem. C, 115 (2011), 9806.

[77] L. Tzabari, N. Tessler, J. Appl. Phys., 109 (2011), 064501.

[78] M. Kuik, H.T. Nicolai, M. Lenes, G.A.H. Wetzelaer, M. Lu, P.W.M. Blom, Appl. Phys. Lett., 98 (2011), 093301.

[79] A. Kumar, H.H. Liao, Y. Yang, Org. Electron. 10 (2009), 1615.

[80] B.T. D. Villers, C.J. Tassone, S.H. Tolbert, B.J. Schwartz, J. Phys. Chem. C, 113 (2009), 18978.

[81] W. Tress, A. Petrich, M. Hummert, M. Hein, K. Leo, M. Riede, Appl. Phys. Lett., 98 (2011), 063301.

[82] G. Li, V. Shrotriya, Y. Yao, J. Huang, Y. Yang, J. Mater. Chem., 17 (2007), 3126.

[83] J.D. Kotlarski, D.J.D. Moet, P.W.M. Blom, J. Polym. Sci. Part B: Polym. Phys., 49 (2011), 708.

[84] A. Benninghoven, Angew. Chem. Int. Ed. Engl., 33 (1994), 1023.

[85] A. Geiser, B. Fan, H. Benmansour, F. Castro, J. Heier, B. Keller, K.E. Mayerhofer, F. Nüesch, R. Hany, Sol. Energy Mater. Sol. Cells, 92 (2008), 464.

[86] J. You, L. Dou, K. Yoshimura, T. Kato, K. Ohya, T. Moriarty, K. Emery, C. C. Chen, J. Gao, G. Li and Y. Yang, Nature Communications, 4 (2013), 1446.

[87] G. Juska, K. Arlauskas, M. Viliunas and J. Kocka, Phys. Rev. Lett., 84 (2004), 4946.

[88] C. Deibel, A. Baumann and V. Dyakonov, Appl. Phys. Lett., 93 (2008), 163303.

[89] R. Hanfland, M. A. Fischer, W. Brütting, U. Würfel, and R. C. I. MacKenzie, Appl. Phys. Lett., 103 (2013), 063904.

[90] A. Kadashchuk, A. Vakhnin, Y. Skryshevski, V. Arkhipov, E. Emelianova and H. Bässler, Chem. Phys., 291 (2003), 243.

[91] N. V. Malm, R. Schmechel, H. Von Seggern, Synthetic Metals, 126 (2002), 87-95.

[92] J. Steiger, R. Schmechel, H. Von Seggern, Synthetic Metals, 129 (2002), 1-7.

[93] D. V. Lang, J.App. Phys., 45 (1974), 3023.

[94] K. Kawanoa, R. Pacios, D. Poplavskyy, J. Nelson, D. D. C. Bradley, J. R. Durrant, Solar Energy Materials and Solar Cells, 90 (2006), 3520–3530.

[95] A. Guerrero, P. P. Boix, L. F. Marchesi, T. Ripolles-Sanchis, E. C. Pereira, G. Garcia-Belmonte, Solar Energy Materials and Solar Cells, 100 (2012), 185–191.

[96] T. Offermans, S. C. J. Meskers and R. A. J. Janssen, Organic Electronics, 7 (2006), 213–221.

[97] I. Hwang, C. R McNeill, N. C. Greenham, J. Appl. Phys., 106 (2009), 094506.

[98] Y. T. Set, M. D. Heinemann, E. Birgersson and J. Luther, J. Phys. Chem. C, 117 (2013), 7993−8000.

[99] M. T. Neukom, N. A. Reinke, B. Ruhstaller, Sol. Eng., 85 (2011), 1250-1256.

[100] L. J. A. Koster, E. C. P. Smits, V. D. Mihailetchi and P. W. M. Blom, Phys. Rev. B, 72 (2005), 085205.

[101] S. Trotzky, T. Hoyer, W. Tuszynski, C. Lienau, and J. Parisi, J. Phys. D: Appl. Phys., 42 (2009), 055105.

[102] I. Hwang, D. Moses, and A. J. Heeger, J. Phys. Chem. C, 112 (2008), 4350-4354.

[103] S. De, T. Pascher, M. Maiti, K. G. Jespersen, T. Kesti, F. Zhang, O. Inganas, A. Yartsev, V. Sundstrom, J. Am. Chem. Soc., 129 (2007), 8466−8472.

[104] S. K. Pal, T. Kesti, M. Maiti, F. Zhang, O. Inganas, S. Hellstrom, M. R. Andersson, F. Oswald, F. Langa, T. Osterman, J. Am. Chem. Soc., 132 (2010), 12440−12451.

[105] J. Piris, T. E. Dykstra, A. A. Bakulin, P. H. M. V. Loosdrecht,W. Knulst, M. T. Trinh, J. M. Schins, and L. D. A. Siebbeles, J. Phys. Chem. C, 113 (2009), 14500–14506.

[106] M. M. Mandoc, F. B. Kooistra, J. C. Hummelen, B. D. Boer, P. W. M. Blom, Appl. Phys. Lett., 91 (2007), 263505.

[107] T. Kirchartz, B. E. Pieters, J. Kirkpatrick, U. Rau, J. Nelson, Phys. Rev. B, 83 (2011), 115209.

[108] M. Kuik, L. J. A. Koster, G. A. H. Wetzelaer, P. W. M. Blom, Phys. Rev. Lett., 107 (2011), 256805.

[109] K. Seki, K. Marumoto and M. Tachiya, Jpn. J. Appl. Phys., 53 (2014), 01AB13.

[110] T. Zhang, E. Birgersson, K. Ananthanarayanan, C. H. Yong, L. N. S. A. Thummalakunta and J. Luther, J. Appl. Phys., 112 (2012), 084511.

[111] L. J. A. Koster, V. D. Mihailetchi, M. Lenes, and P. W. M. Blom, *Organic Photovoltaics*, edited by C. Brabec, V. Dyakonov, and U. Scherf (Wiley-VCH Verlag GmbH & Co. KGaA, Weinheim, 2009), pp. 283–298.

[112] V. Turkovic, S. Engmanna, D. A. M. Egbe, M. Himmerlich, S. Krischok, G. Gobsch, H. Hoppe, Solar Energy Mater. Solar Cells, 120 (2014), 654–668.

[113] Y. Roichman and N. Tessler, Appl. Phys. Lett., 80 (2002), 1948–1950.

[114] D. Taguchia, T. Shinoa, X. Chena, L. Zhanga, J. Lia, M. Weisb, T. Manakaa, M. Iwamotoa, Appl. Phys. Lett., 98 (2011), 133507.

[115] C. Vijila, S. P. Singh, E. Williams,P. Sonar, A. Pivrikas, B. Philippa, R. White, E. N. Kumar, S. G. Sandhya, S. Gorelik, J. Hobley, A. Furube, H. Matsuzaki and R. Katoh, J. Appl. Phys., 114 (2013), 184503.

[116] Vaidotas Kažukauskas, Vidmantas Kalendra, Juozas-Vidmantis Vaitkus, Materials Science (Medžiagotyra)., 11 (2005),1392-1320.

[117] T. Yamanari, T. Taima, J. Sakai, J. Tsukamoto and Y. Yoshida, Jpn. J. Appl. Phys., 49 (2010), 01AC02.

[118] K. H. Wong, K. Ananthanaranayan, P. Balaya, J. Phys. Chem. C, 116 (2012), 16346.

[119] F. J. Lim, K. Ananthanarayanan, J. Luther and G. W. Ho, J. Mater. Chem., 22 (2012), 25057-25064.